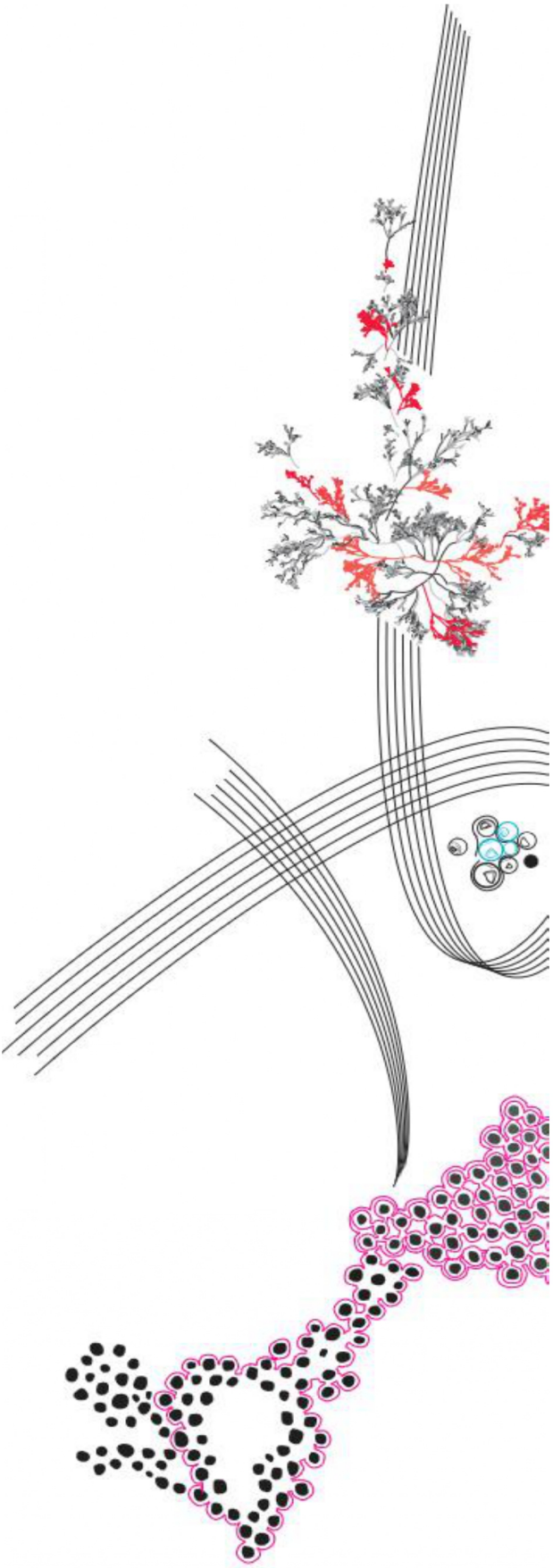

MSc Thesis

MAGNETICALLY-ACTUATED SOFT ROBOTS WITH SELECTIVE THERMAL ACTIVATION FOR COLLABORATIVE MOTION

M. Kaddouri

FACULTY OF ENGINEERING TECHNOLOGY
DEPARTMENT OF BIOMECHANICAL ENGINEERING

EXAMINATION COMMITTEE

Dr. V. Kalpathy Venkiteswaran

Dr. A. Sadeghi

December 10th, 2025

Thesis submitted by
Miryam Kaddouri
under the supervision of
Dr. Venkat Kalpathy Venkiteswaran, and
Dr. A. Sadeghi
in order to fulfill the necessary requirements to obtain a Master's degree in
Robotics Engineering
at the University of Twente
and defended on
Wednesday, 10th of December, 2025

Acknowledgement

The work presented in this thesis is the result of approximately nine months of research at the Surgical Robotics Laboratory (SRL) at the University of Twente. I am grateful for the opportunities, support, and guidance I received throughout this period. Though the work was challenging, I genuinely enjoyed the process of bringing it from concept to demonstration.

I would like to express my sincere gratitude to my supervisor, Dr. Venkat Kalpathy Venkiteswaran, for his invaluable guidance. His critical feedback was particularly useful, often providing a new perspective that helped me unlock difficult problems. His insights, combined with the freedom to explore my own ideas, pushed me to refine my work at every stage.

I am deeply thankful to the members of the Surgical Robotics Laboratory for creating a collaborative environment. I especially acknowledge Dr. Nicholas Posselli for being attentive and willing to assist with COMSOL simulations, and Simon Frieler for his helpful tips on materials. I am very grateful to Lukas Masjosthusmann, who was always proactive in asking how the work was progressing and offering help with both simulations and experiments. A special thanks to Dr. Chen Wang for our planned discussions; his feedback on my approach and suggestions for literature were incredibly beneficial. I also thank Mohammad Ebrahim Imanian for his assistance in the workshop and for keeping the environment friendly, and Dr. Ali Sadeghi for his constructive feedback on my presentation during the Greenlight meeting.

My appreciation extends to the technical staff, particularly Quint Meinders, for his readiness to troubleshoot issues with 3D printing and laser cutting whenever needed.

I am profoundly grateful to my family, especially my sister Samia, who has been my strongest support and always by my side throughout this entire process. Finally, I thank my friends and classmates for their encouragement during the challenging phases of this work.

Miryam Kaddouri
December 10th, 2025

Abstract

Minimally invasive medical procedures hold promise for transformation through small-scale robotic systems, yet current magnetic soft robots face a fundamental challenge: global magnetic fields do not lend themselves well to the independent control of individual robots during multi-robot assembly. Existing solutions often sacrifice the soft, biocompatible form factor or accept limited control authority within swarms. This work addresses this challenge through dual-stimulus control, combining global magnetic actuation with thermally reversible adhesion for selective anchoring. The objective is to demonstrate that magnetically actuated soft robots can achieve selective locking, unlocking, and cooperative motion by integrating external RF heating with a thermally reversible adhesive interface. This approach relies on a specific force hierarchy ($F_{\text{adh,cold}} > F_{\text{magnetic}} > F_{\text{adh,hot}}$) that enables individual robots to be selectively anchored while neighbouring robots are manipulated, then released on demand through localised thermal activation.

To validate this principle, hexagonal soft robots were fabricated with an asymmetric magnetic polarity configuration and compliant hinges that enable controlled deformation. Systematic experimental characterisation quantified the magnetic interaction forces, thermal activation performance, and adhesion strength. Results established a robust force hierarchy where cold-state adhesion (5.40 ± 0.13 N normal, 7.21 ± 0.46 N shear) substantially exceeds the maximum magnetic coupling forces (3.5 N peak at near-contact), while hot-state adhesion drops to near zero above 80°C. Integrated proof-of-concept demonstrations validated the selective control capabilities across progressively complex scenarios, including single-robot locking/unlocking, multi-robot line and ring assembly, and collective rotation under uniform magnetic fields. This work establishes that dual-stimulus control enables selective, on-demand reconfiguration of multi-robot assemblies, providing a foundation for future reconfigurable soft robotic systems capable of sequential assembly and cooperative motion.

Table of Contents

List of Abbreviations

RF	Radio Frequency
PLA	Polylactic Acid
TPU	Thermoplastic Polyurethane
SMP	Shape Memory Polymer
PCL	Polycaprolactone
CAD	Computer-Aided Design
EVA	Ethylene-Vinyl Acetate
FDM	Fused Deposition Modeling
MPC	Magnetic Polymer Composite
NdFeB	Neodymium Iron Boron
NIR	Near-Infrared
PDMS	Polydimethylsiloxane

List of Figures

List of Tables

1 Introduction

Magnetically actuated soft robots have emerged as promising candidates for locomotion and manipulation in constrained or delicate environments due to their compliance, wireless actuation capability, and ability to navigate complex geometries [2, 9, 10]. Their motion is typically controlled by externally applied magnetic fields, which provide precise steering and enable untethered operation at millimetre and sub-millimetre scales. These characteristics have motivated applications such as targeted drug delivery, tissue interaction, and gastrointestinal navigation [11, 12]. However, a key limitation persists: magnetic fields are inherently global. When multiple robots share the same workspace, they all experience the same magnetic forces and torques, making selective control of individual robots one of the central challenges in magnetic swarm robotics [13, 14].

Several strategies have been proposed to achieve selective control, including geometric differentiation, resonant-frequency tuning, and tailored magnetisation patterns [15,16]. While these approaches demonstrate partial selectivity, they do not scale well to larger robot collectives and often require strict fabrication tolerances or highly specific control inputs. Recent studies therefore increasingly combine magnetic actuation with secondary, spatially addressable stimuli, such as optical, thermal, or chemical activation to enable localised behaviours within globally applied magnetic fields [12,17,18]. These works highlight that achieving independent behaviour within a global field requires a second modality that can be applied locally.

This thesis builds upon this concept by introducing a dual-stimulus mechanism that integrates magnetic mobility with thermally reversible adhesion. The robots developed in this work are modular hexagonal units containing three asymmetrically arranged, embedded neodymium magnets. This configuration yields a well-defined net magnetic dipole moment, enabling predictable alignment and allowing multiple robots to mechanically assemble into lines or rings under global fields. To introduce selectivity, the robots interact with an EVA-based thermoplastic adhesive layer that can reversibly transition between strong and weak adhesion states depending on its temperature. Local heating is achieved using externally applied radio-frequency (RF) induction, enabling a single robot to be anchored while neighbouring robots remain fully mobile under the same magnetic field. When reheated above the EVA softening temperature ($\sim$ 80–90°C), the anchored robot detaches without requiring any change to the magnetic control input. Figure 1 illustrates the complete selective locking–unlocking sequence.

The objective of this thesis was to design, fabricate, and experimentally validate magnetic soft-robots capable of selective thermal activation. The research included: (i) development of the three-magnet asymmetric configuration for deterministic dipole-driven assembly; (ii) a thermal parameter study of the EVA–foil interface; (iii) magnetic force measurements and COMSOL simulations to characterise magnet–magnet interactions between robots; and (iv) demonstration of selective anchoring, multi-robot line and ring formation, and collective rotation of ring assemblies under uniform magnetic fields. Together, these contributions establish a proof-of-concept system in which magnetically mobile soft robots can attach, detach, and reconfigure selectively within a shared global magnetic field.

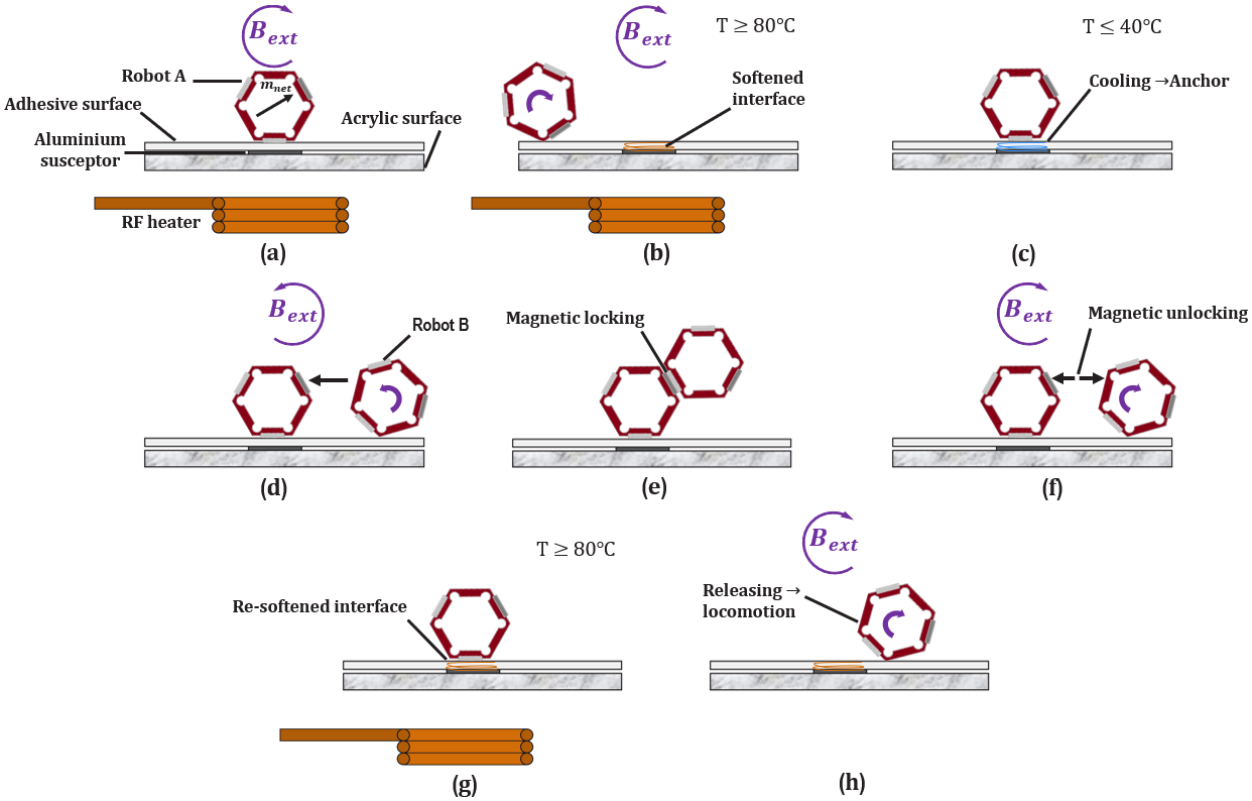

Figure 1: Sequential illustration of the selective magnetic–thermal activation principle. (a) **System overview:** A hexagonal robot with a programmed net magnetic dipole ($\mathbf{m}_{\text{net}}$) operates on an acrylic substrate coated with an EVA adhesive layer and aluminium susceptor. Global magnetic fields (B_{ext}) provide locomotion, while the RF heater enables localised thermal activation for selective anchoring. (b) **Local softening for targeted anchoring:** The RF heater raises the temperature of a selected region above the EVA softening point ($T \geq 80°\text{C}$), allowing Robot A to be guided to the softened spot. (c) **Anchoring after cooling:** Once Robot A is positioned, the EVA cools to $T \leq 40°\text{C}$ and forms a strong adhesive interface that anchors Robot A while preserving its magnetic responsiveness. (d) **Magnetic locking of a second robot:** Under a global magnetic field, Robot B can be steered toward the anchored Robot A and magnetically lock to it without disturbing the anchor. (e) **Two-robot assembly:** The robots form a stable magnetic connection, demonstrating controlled assembly around the anchored unit. (f) **Selective magnetic unlocking:** By reversing the magnetic pulling direction, Robot B can be magnetically unlocked from Robot A, which remains immobilised due to the cold-state EVA adhesion. (g) **Thermal release of the anchored robot:** Local reheating beneath Robot A softens the EVA again ($T \geq 80°\text{C}$), removing the adhesion constraint. (h) **Reactivation and locomotion:** With the adhesion eliminated, the global magnetic field can re-engage and reposition Robot A, completing the selective locking–unlocking sequence.

2 Background and literature

This chapter describes the theoretical and technical background for developing magnetically actuated soft robots with selective thermal activation. It establishes the current state of magnetic actuation technology, identifies the core challenge of selective control in robot swarms, examines thermal activation as a solution approach, reviews adhesive mechanisms for implementation, and identifies the research gap motivating this work.

2.1 Magnetic soft robots

Magnetic soft robots are deformable robotic systems composed of elastomeric or polymeric matrices embedded with magnetic particles that enable remote actuation through external magnetic fields. These magnetic polymer composites (MPCs) convert magnetic field energy into mechanical motion while maintaining compliance and adaptability [2,10,19]. The contactless nature of magnetic actuation allows untethered operation and high precision in confined or delicate environments, which is particularly advantageous for biomedical applications such as targeted drug delivery, tissue manipulation, and minimally invasive procedures [8,11,12].

Magnetic soft robots are typically classified according to the type of magnetic fillers used in their composite matrix. *Soft-magnetic* materials such as iron, nickel, and Fe_3O_4 exhibit field-dependent magnetisation that allows fast, reversible deformation under external fields, while *hard-magnetic* materials such as NdFeB retain programmed magnetisation, enabling pre-defined shape morphing and persistent magnetic memory [2, 19]. These fillers are dispersed within flexible matrices such as PDMS, silicone rubber, or thermoplastic polyurethane (TPU), which offer mechanical resilience and large-strain capability [1, 2]. The magnetisation direction can be encoded during fabrication by field-assisted curing or mechanical alignment, creating spatially varying magnetisation patterns that give rise to controlled shape changes and locomotion modes [2, 17].

Recent studies have demonstrated a wide range of MPC-based robotic systems exhibiting rolling, swimming, crawling, and bio-inspired deformation. Ren *et al.* [1] presented a reprogrammable small-scale magnetic soft-bodied robot with multimodal locomotion, combining rolling and flipping motions through encoded magnetisation. Miao *et al.* [2] reviewed the functionalisation of magnetic robots with life-like morphologies such as graspers and inchworm-like crawlers. Wang *et al.* [11] developed a mucoadhesive magnetic film capable of adhering to biological tissue for controlled locomotion. Chen *et al.* [8] introduced a multilayer magnetic soft robot with selective adhesion properties for targeted attachment and release. Siebenmorgen *et al.* [12] demonstrated thermo-magnetic dual-responsive soft robots designed for complex shape changes in medical environments. Collectively, these systems show how embedded magnetic particles enable autonomous, compliant, and multifunctional actuation within soft polymer matrices. Figure 2 illustrates representative locomotion modes realised by magnetic soft robots, including rolling, walking and tumbling behaviours achieved under external magnetic fields.

Magnetic actuation systems can be broadly divided into permanent-magnet setups and electromagnetic coil platforms. Permanent magnets are compact and easily reconfigurable, generating static or rotating gradient fields suitable for translation and alignment. Electromagnetic coil systems, as reviewed by Yang and Zhang [9] and Ebrahimi *et al.* [10], enable programmable field control with six degrees of freedom and allow dynamic modulation of field strength and direction. Large-scale systems such as the six-coil setup described by Venkiteswaran and Misra [20] have demonstrated precise control over small soft robots, while smaller portable magnetic arrays have been used for swarm navigation and cooperative manipulation [13,14]. Figure 3 summarises the main classes of magnetic actuation systems used in soft robotics. Permanent-magnet setups generate strong spatial gradient fields that are well suited for translation and alignment but offer limited independent control when multiple robots share the same field. In contrast, electromagnetic coil systems provide programmable uniform or rotating fields with precise modulation of field strength and direction, enabling multi-DOF control, cooperative manipulation, and closed-loop feedback strategies [9,10]. This distinction is central to understanding how different actuation platforms affect locomotion capabilities, workspace constraints, and scalability.

Despite these advances, magnetic actuation remains inherently global where every robot within the same field experiences identical magnetic forces and torques. This coupling limits individual addressability, a critical requirement for swarm coordination or cooperative manipulation tasks. Earlier strategies for

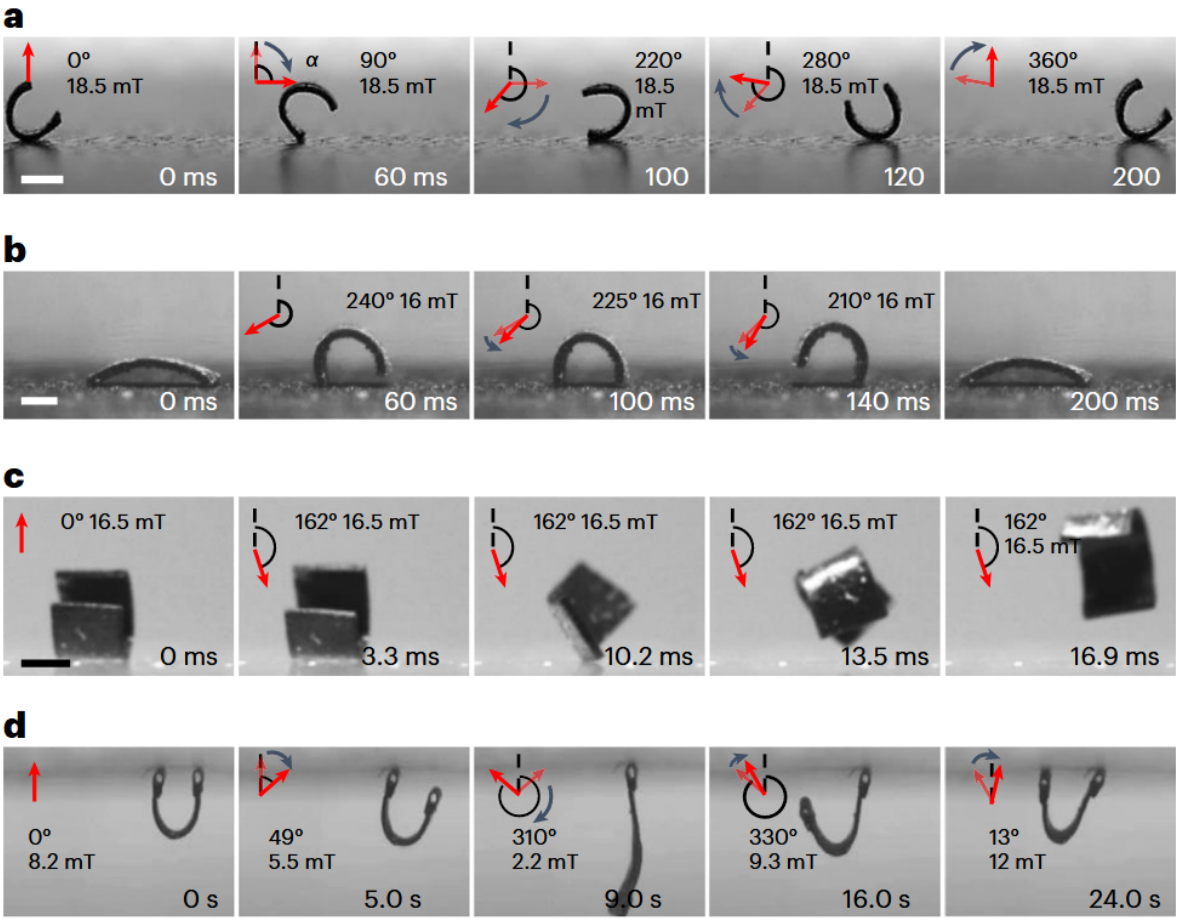

Figure 2: Examples of magnetic sheet-shaped robot soft robots fabricated from magnetic polymer composites, demonstrating a, Rolling. b, Walking. c, Jumping. d, Tumbling-based climbing, behaviours under external magnetic fields [1]

selective magnetic control included superimposing oscillating fields or using robots with different magnetic signatures [15, 16], but scalability and precision remain challenging. Wang *et al.* [14] recently reviewed methods for achieving independent microrobot control, emphasising the limitations of purely magnetic means. To overcome this constraint, researchers have begun integrating magnetic actuation with secondary stimuli, such as thermal, optical, or chemical activation to introduce spatial selectivity without losing the advantages of magnetic locomotion [12, 17]. The present thesis builds upon this approach by introducing thermal activation as a secondary control modality to achieve selective locking and unlocking of magnetically coupled soft robots.

2.2 Selective activation in swarms

Individual robot control in magnetic swarms faces a fundamental challenge because all units respond to the same global magnetic field. Wang *et al.* highlighted that despite extensive efforts in independent microrobot control, scalability and selectivity remain open challenges [14]. These efforts used global fields, frequency tuning, and localised actuation. This limitation restricts the potential for collaborative behaviours that require individual robot addressing.

Floyd *et al.* demonstrated selective control using differences in magnetisation, shape demagnetisation, and rotational inertia, achieving discriminated motion in small groups [13]. However, they acknowledged scalability limitations, and their work validates the need for alternative selectivity approaches beyond purely

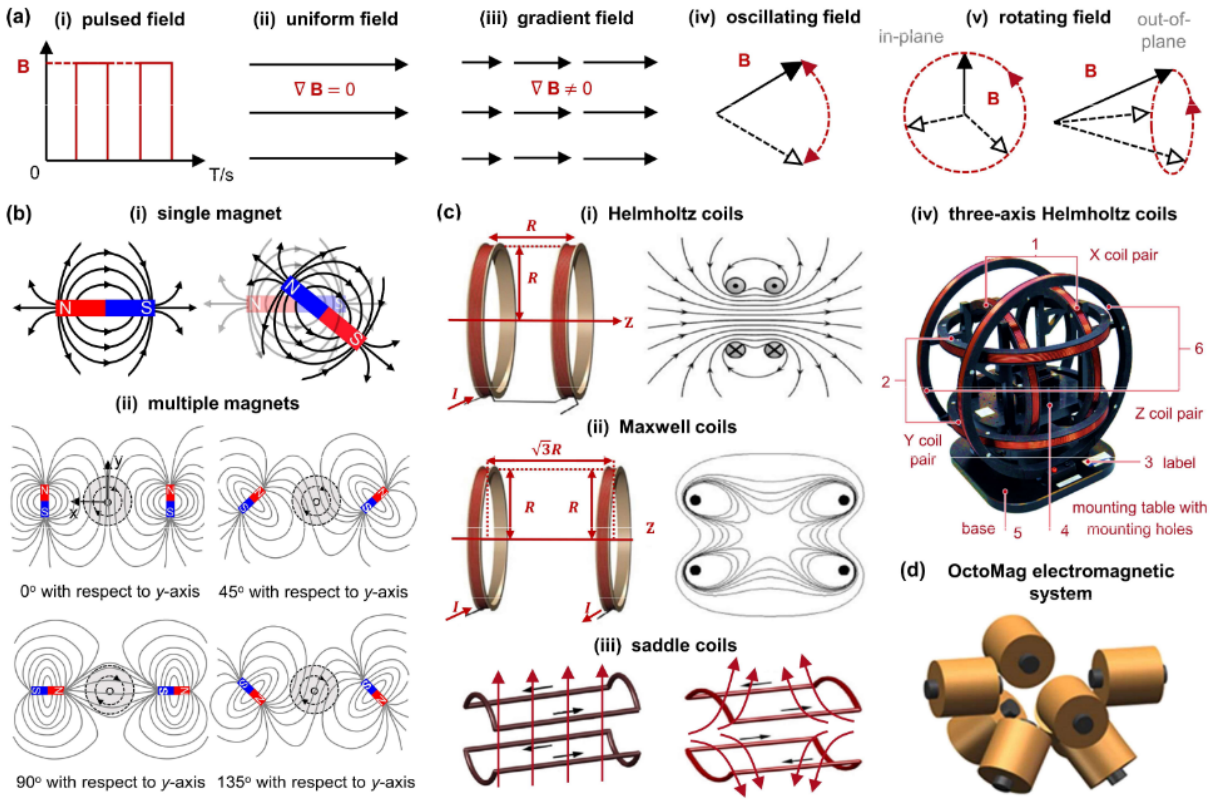

Figure 3: (a) Several standardized types of magnetic fields. (b) Permanent magnet systems: (i) a single magnet; (ii) multiple magnets. (c) Orthogonal paired coils: (i) Helmholtz coils; (ii) Maxwell coils; (iii) saddle coils; (iv) three-axis Helmholtz coils. (d) Distributed electromagnets: OctoMag electromagnetic actuation system [2]

magnetic differentiation.

Tottori *et al.* explored selective control through geometric differences and resonant frequency tuning for multiple magnetic helical microrobots [15]. They found these methods become impractical as swarm size increases due to precise geometric manufacturing requirements and limited distinguishable frequency bands. Research on independent positioning of magnetic nanomotors showed similar scalability constraints that increase as the number of robots grows [16].

The core limitation stems from the global nature of magnetic fields where any field strong enough to actuate one robot inevitably affects all other magnetic robots within the workspace. Both Floyd *et al.* and Wang *et al.* acknowledged that current approaches using global fields face unresolved scalability challenges [13, 14]. This led researchers to explore alternative approaches that combine magnetic actuation with additional stimulus modalities.

Figure 4 conceptually illustrates this limitation: when a single global magnetic field is applied, every robot within the workspace experiences the same magnetic forces and torques, making individual addressing inherently difficult. Even with differences in geometry, magnetisation, or resonance, all robots remain fundamentally coupled to the same field input, which constrains scalability in larger swarms.

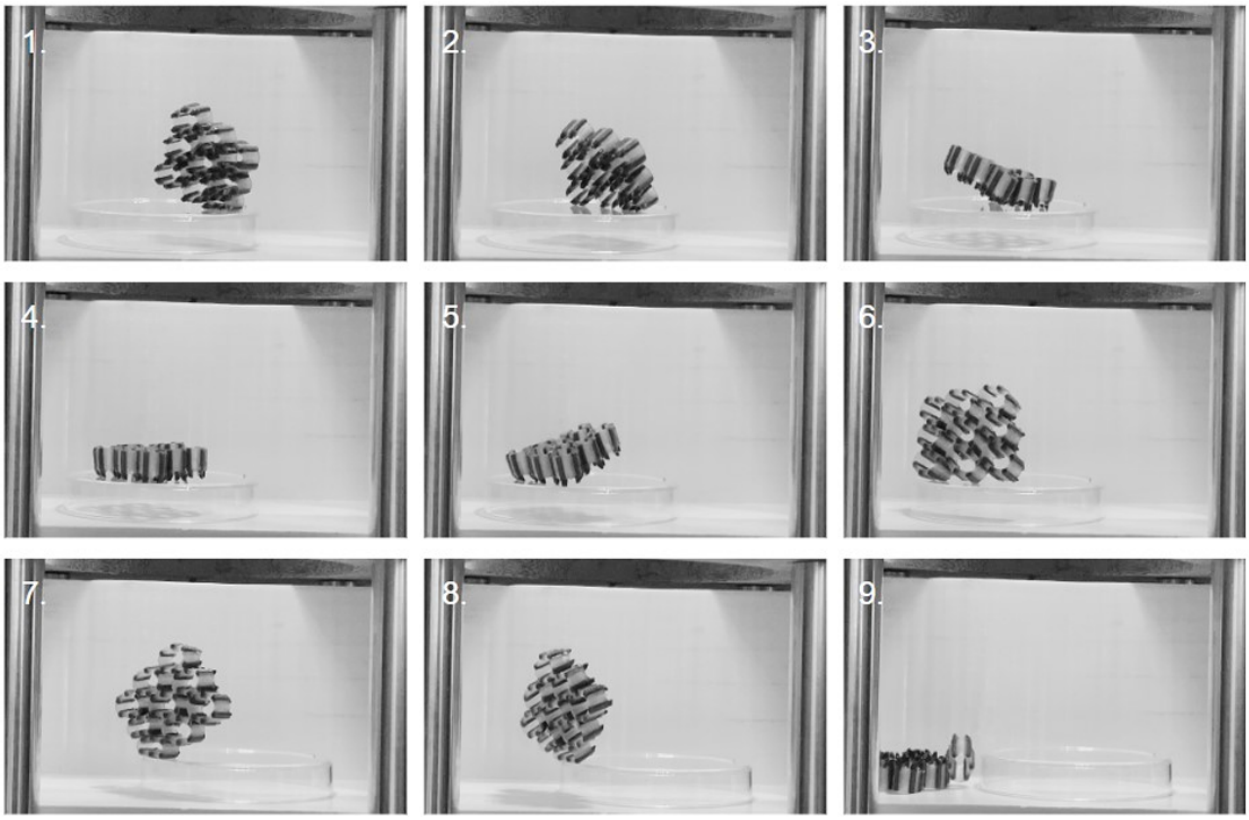

Figure 4: Illustration of the global-field limitation in magnetic swarms, where all robots within the workspace respond identically to a single magnetic field [3]

2.3 Thermally responsive materials and mechanisms

Thermally responsive materials exhibit temperature-dependent transitions that reversibly alter their stiffness, shape, or adhesion properties. They provide an additional control dimension for soft robotic systems, one that operates independently from magnetic actuation. When combined with magnetic mobility, these materials enable selective activation, where magnetic fields remain global but heating can be applied locally to target individual robots or interfaces [10, 21].

A variety of materials display thermally induced transitions that can be exploited in soft robotics. *Shape-memory polymers* (SMPs), such as polyurethane and polycaprolactone (PCL), undergo reversible deformation recovery when heated above their glass transition or melting temperature, allowing reconfigurable or self-locking structures [21]. *Thermoplastic adhesives* like ethylene-vinyl acetate (EVA) soften upon heating and resolidify during cooling, offering fast, repeatable, and reversible adhesion useful for robotic assembly tasks. *Thermoresponsive hydrogels*, such as poly(N-isopropylacrylamide) (pNIPAm), exhibit volumetric contraction above their lower critical solution temperature (LCST), enabling stiffness modulation and shape locking [12]. These classes differ in activation temperature, response speed, and reversibility, allowing designers to tune their behaviour according to the robot's functional needs.

Thermal activation in soft robots can be achieved through multiple energy transfer methods. Direct techniques include resistive (Joule) heating via conductive traces and convective heating using hot air or infrared sources. Indirect, wireless techniques rely on energy conversion such as *photothermal* or *inductive* heating. Photothermal activation converts absorbed light (often from near-infrared or laser sources) into local heat through light-absorbing coatings or embedded nanoparticles. This approach enables sub-millimetre spatial selectivity and has been widely applied in microrobotics [17,18]. Inductive (RF) heating, on the other hand, relies on electromagnetic coupling with metallic or magnetic susceptors (e.g., aluminium or iron foils), providing distributed but contactless activation suitable for macroscale or swarm applications. The choice

of heating method depends on desired localisation, energy efficiency, and compatibility with the surrounding medium [1, 2].

Coupling magnetic and thermal stimuli combines the strengths of both modalities: magnetic fields provide remote locomotion and alignment, while thermal inputs enable spatially selective softening, locking, or unlocking. This dual-stimulus concept allows multiple robots to coexist within a shared magnetic workspace yet be individually addressable through local heating [12, 17]. Zhao *et al.* demonstrated programmable, addressable shape changes in magnetic helical microrobots using laser-based photothermal activation, achieving independent control for units spaced only 800 µm apart [18]. Liu *et al.* further validated magneto-thermal coupling by demonstrating soft composites capable of dual-mode actuation where magnetic and photothermal inputs function independently without interference [17]. Siebenmorgen *et al.* integrated pNIPAm hydrogels with ferromagnetic particles to realise thermo-magnetic dual-responsive soft robots that can reversibly change stiffness and shape under heating, demonstrating lock–unlock behaviours suitable for manipulation tasks [12].

Recent work by Soon *et al.* [4] provides important design guidelines for RF-based heating that directly inform the material and geometric choices in this thesis. Their study showed that Joule heating efficiency depends strongly on both the thickness of the metallic susceptor and its distance from the RF coil. Thin metallic layers (< 50 µm) exhibited faster rise times but lower peak temperatures, whereas thicker foils (50–100 µm) generated substantially higher heating due to larger induced eddy currents. However, foil thicknesses above 100 µm introduced diminishing returns because the skin depth at 338 kHz limits current penetration. In addition, heating performance decreases rapidly with distance: a five-fold increase in coil–sample separation reduced achievable temperatures more than an order of magnitude, confirming that magnetic flux density dominates over convective losses. These insights highlight the critical trade-off between localisation, heating rate, and mechanical integration when selecting foil thickness and coil placement.

Together, these studies establish thermal activation as a robust method for achieving spatial selectivity in magnetically actuated systems. By leveraging programmable materials and controlled heating, robots can switch between rigid and compliant states or adhesive and non-adhesive modes. The next subsection explores thermally reversible adhesives, specifically EVA-based interfaces as a practical implementation for lock–unlock behaviour in modular magnetic robots. Figure 5 summarises representative thermal activation strategies that have been employed in soft robotic systems. These examples highlight the some of the available heating modalities, from wireless inductive heating to photothermal and resistive (Joule) heating, and how each enables localisation or selective material activation. Together, they illustrate a practical design space for integrating thermal stimuli with magnetic actuation in multi-functional soft robots.

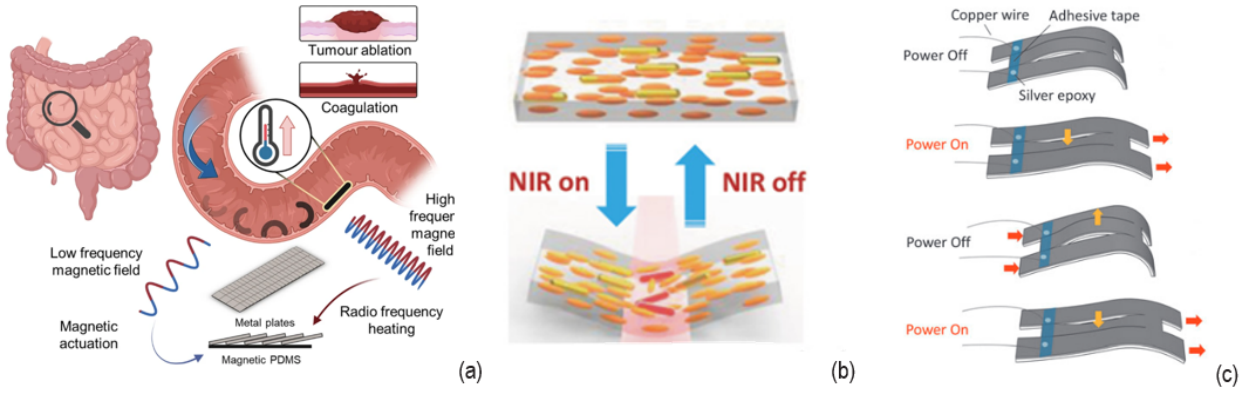

Figure 5: Representative thermal activation mechanisms used in soft robotics: (a) RF induction heating via metallic foil [4], (b) NIR photothermal laser heating [5], (c) Joule heating through conductive traces [6].

2.4 Adhesive mechanisms for locking and unlocking

Collaborative robot functionality requires reversible bonding mechanisms that enable dynamic joining and separation of robots. Thermally controlled adhesion offers an effective approach for achieving selective mechanical coupling between robots while maintaining the ability to reconfigure system topology on demand. By exploiting temperature-dependent transitions in adhesive materials, inter-robot bonds can be engaged or released in a controlled and repeatable manner.

Thermal control of adhesion can be realised using materials that transition between solid and viscous states upon heating. A notable example is the polycaprolactone–epoxy (PCL–epoxy) composite system described by Luo *et al.*, which achieves reversible bonding through differential expansive bleeding (DEB) [7]. In this system, PCL melts at approximately 60 °C to provide strong adhesion (up to 2.3 MPa) that can be thermally released upon reheating. The adhesive exhibits a "bricks-and-mortar" microstructure in which rigid epoxy spheres are embedded within a PCL matrix. When heated, the molten PCL flows to wet the contact surface, and upon cooling, recrystallises to form a solid joint. This cycle can be repeated multiple times with minimal performance degradation, demonstrating excellent stability for multi-use robotic systems.

An alternative approach was demonstrated by Chen *et al.*, who developed a magnetic multi-layer soft robot incorporating hydrogel films to achieve targeted adhesion [8]. Their system allowed reversible bonding through controlled layer separation driven by magnetic torque. Although this approach demonstrated selective adhesion and compatibility in biological environments, it lacked thermal responsiveness and therefore relied solely on magnetic field configurations for control. The absence of thermal activation limits spatial precision and selectivity in multi-robot systems where independent actuation is required.

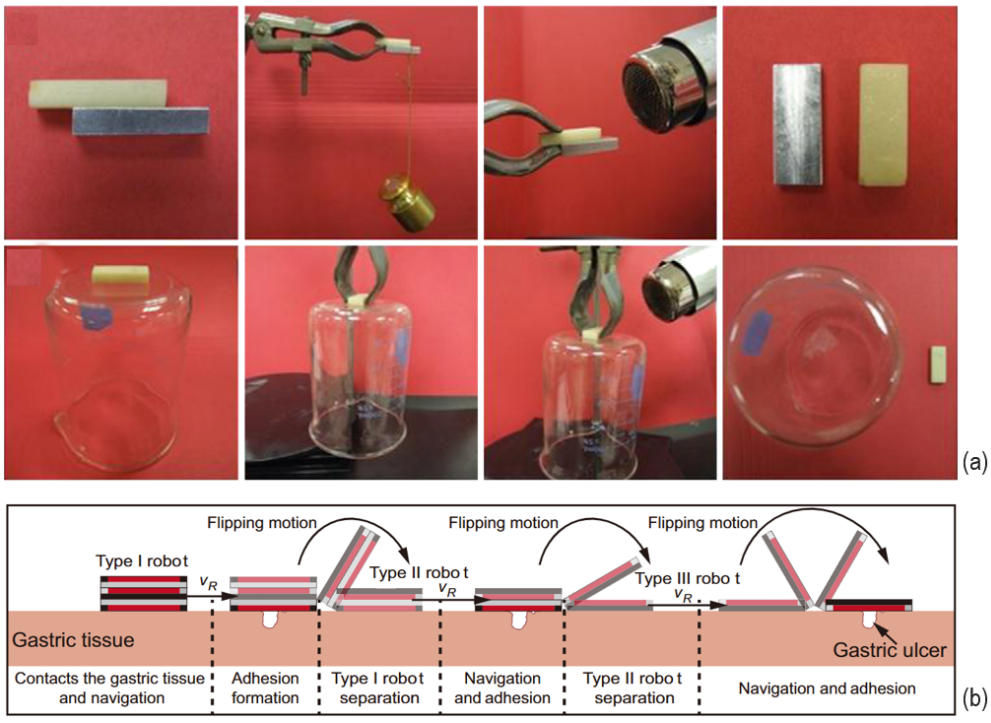

Figure 6: Comparative mechanisms of reversible adhesion. (a) PCL–epoxy composite adhesive: rigid epoxy "bricks" embedded in a polycaprolactone matrix that melts above 60 °C, enabling reversible wetting and recrystallisation-based bonding [7], (b). Magnetic multilayer soft robot: hydrogel film provides reversible adhesion under magnetic torque-driven layer separation [8].

Thermal activation provides several advantages over purely mechanical or magnetic separation methods. It enables remote, contactless control of adhesive states and allows energy input to be tuned through temperature and duration of heating. This permits both simultaneous release of multiple bonds and selective unlocking of individual connections. However, thermally controlled adhesion systems must balance several

design factors, including temperature compatibility with surrounding materials, achievable heating rates, and the repeatability of adhesion strength over multiple cycles.

Overall, thermally reversible adhesives present a promising strategy for selective mechanical coupling in modular robotic systems. When combined with magnetic actuation, they provide the dual capability of global motion and localised connection control forming the foundation for the lock–unlock mechanism developed in this work. Figure 6 summarises two representative strategies for reversible adhesion that have been explored in soft robotics. These examples highlight the range of material–based mechanisms that enable lock–unlock behaviour, from thermally driven wetting and recrystallisation in polymer composites to magnetically induced layer separation in multilayer structures. Together, they illustrate how reversible bonding can be engineered through either thermal or magnetic stimuli depending on the application context.

2.5 Summary of the state of the art

The literature demonstrates significant progress in magnetic actuation for soft robotics, establishing it as a mature technology platform that enables wireless control, biocompatibility, and precise manipulation. However, despite its versatility, achieving scalable and selective control within magnetic robot swarms remains an unresolved challenge. Existing strategies for selectivity, such as differentiation by geometry, magnetic properties, or resonant frequency, offer limited scalability because they rely on static design features or a finite number of controllable frequency bands. These approaches become increasingly impractical as swarm size grows and do not provide dynamic reconfigurability once the robots are deployed. Furthermore, complex magnetic field configurations can manipulate multiple robots simultaneously but fail to achieve true independent control, as all magnetic bodies within a shared workspace experience the same global field.

Integrating thermally responsive materials with magnetic actuation introduces an orthogonal control dimension that can overcome these scalability limitations by enabling selective activation at the material level. Thermal inputs can be spatially localised and temporally controlled, allowing individual robots to switch between active and inactive states without affecting neighbouring units. Recent work by Zhao *et al.* and Siebenmorgen *et al.* validates this dual-stimulus approach, demonstrating that thermal and magnetic control modalities can operate independently without interference [12, 18]. Building upon these findings, this thesis develops a magnetically actuated soft robotic system incorporating selective thermal activation to achieve controllable locking and unlocking between robots. The proposed approach directly addresses the selectivity gap in current magnetic swarm systems and lays the foundation for scalable, collaborative, and reconfigurable multi-robot behaviour.

3 Methodology

3.1 System concept and objectives

This chapter describes the design and validation of a soft robotic system capable of selective thermal unlocking within a global magnetic field. The central scientific challenge addressed in this work is the global field limitation: in a shared workspace, every magnetic robot responds identically to an external field, making individual control impossible without a secondary localisation mechanism.

To overcome this, the system integrates two independent control stimuli. Global magnetic actuation provides the primary force for locomotion and assembly, while localised thermal activation acts as a secondary selection mechanism. In this architecture, each robot contains embedded permanent magnets for locomotion and inter-robot coupling, and is temporarily anchored to a substrate coated with a thermoplastic Ethylene–vinyl acetate (EVA) layer. By locally heating specific regions of the EVA-coated substrate, the adhesive softens, transitioning the targeted robot from an anchored state to a free state. This thermally gated boundary condition allows specific robots to be actuated by the global field while their neighbours remain mechanically fixed.

To achieve this functionality, the system was designed to meet six specific requirements:

1. *Selective actuation:* A targeted robot must unlock and move while neighbouring robots remain anchored under the same applied magnetic field.

2. *Magnetic locomotion:* Embedded permanent magnets must generate sufficient force and torque for robot–robot coupling, translation under gradient fields and rotation under uniform field.

3. *Reversible adhesion:* The interface must provide strong anchoring in the cold state ($T < 40°\mathrm{C}$) and negligible resistance in the hot state ($T > 80°\mathrm{C}$).

4. *Substantial deformation capability:* The robot body must be capable of reversible shape change exceeding a 50% height reduction under strong magnetic loading to enable shape adaptation in response to external constraints.

5. *Modular reconfigurability:* The robots must be capable of self-assembling into fundamental structures (lines, rings) and reconfiguring via selective detachment.

6. *Cycle repeatability:* The adhesive interface must support multiple heating–cooling cycles without significant degradation.

3.2 Operational principles and design requirements

The operation of the system relies on a specific hierarchy of mechanical forces defined by the thermal state of the adhesive. The robot interacts with two primary magnetic sources: the passive attraction from neighbouring robots (F_{AB}) and the active pull from an external actuation magnet (F_{ext}).

In the cold state, the solid EVA layer exerts an adhesion force ($F_{\mathrm{adh,cold}}$) that fixes the robot to the substrate. This anchor serves two critical mechanical functions. First, it must resist the impact force when a second robot snaps into contact during assembly ($F_{AB,\max}$). Second, and most crucially for reconfigurability, it must withstand the external pull required to detach a neighbouring robot. When the external magnet is applied to peel Robot B away from Robot A, the anchor holding Robot A must not yield.

In the hot state, local heating to approximately 80°C softens the EVA, reducing the interface strength. In this state, the external magnetic field applies not only a translational force but also a torque ($\boldsymbol{\tau} = \mathbf{m}_{\mathrm{net}} \times \mathbf{B}_{\mathrm{ext}}$). This torque rotates the robot, creating a stress concentration at the interface edge. Mechanically, this peeling action requires significantly less force than a direct vertical lift, allowing the targeted robot to detach easily even if the magnetic pull force is moderate.

Figure 7 illustrates this sequence. For the system to function reliably (anchoring against both collisions and neighbour detachment forces when cold, but releasing via peeling when hot) it must satisfy the extended force selectivity condition:

$$F_{\mathrm{adh,cold}} \;>\; \max(F_{AB,\max}, F_{\mathrm{ext}}) \;>\; F_{\mathrm{adh,hot}} \approx 0. \tag{1}$$

This condition ensures that the anchor is stronger than the strongest magnetic disturbance it will encounter, whether from assembly impacts or intentional disassembly manoeuvres.

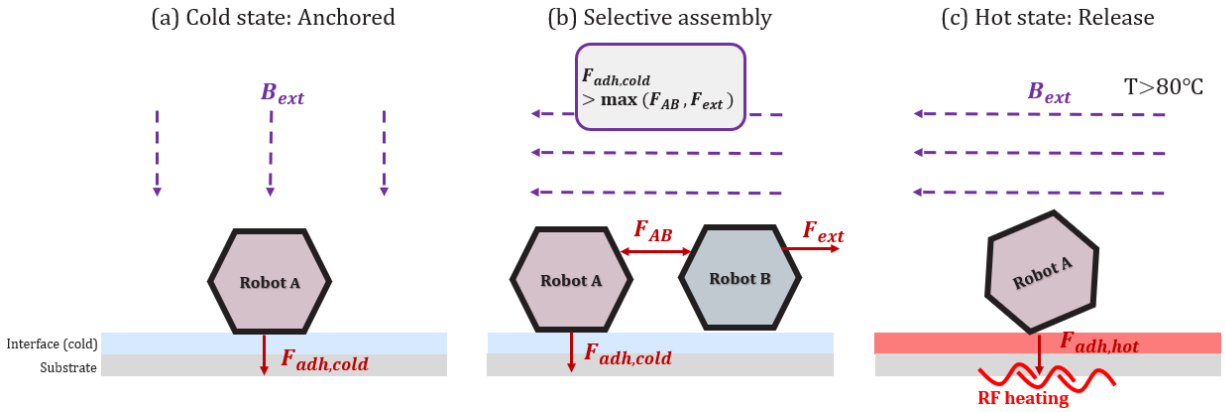

Figure 7: Mechanism of selective thermal unlocking. (a) **Cold state:** The robot is firmly anchored to the substrate by the solid EVA adhesive interface ($F_{\text{adh,cold}}$). (b) **Selective assembly:** The anchor resists the maximum magnetic disturbance, defined as the greater of the inter-robot coupling (F_{AB}) or the external actuation force (F_{ext}). (c) **Hot state:** Local RF heating ($T > 80°\text{C}$) softens the EVA layer, reducing adhesion to near-zero ($F_{\text{adh,hot}}$) and allowing the robot to peel away.

3.2.1 Performance thresholds

To verify the system against Eq. 1, specific design targets were established. Preliminary force measurements conducted during system development (detailed quantitatively in Section 4.1) revealed that the maximum magnetic attraction between two robots at millimeter gaps reaches approximately 3.5 N. To ensure robust anchoring even under worst-case impact loads during dynamic assembly (accounting for both experimental variability and potential transient forces during snap-in), a safety factor of 2.0 was applied. This yields a minimum cold-state adhesion target of greater than 7.0 N. On the other hand, to ensure that torque-induced peeling is successful, the hot adhesion is required to drop to a negligible fraction of the available magnetic force, targeted at less than 0.1 N.

In addition to mechanical constraints, temporal targets were defined to ensure the system is practical for sequential operations. The heating phase must reach the softening point (t_{80}) in under 60 s to align with typical soft robotic actuation timescales. Passive cooling to a rigid state (t_{cool}) is targeted at under 120 s to allow for rapid re-anchoring and cycle repetition.

3.2.2 Experimental validation strategy

The experimental strategy is designed to validate the framework in stages, progressing from component characterisation to full system integration. First, the magnetic interaction forces (F_{AB} and F_{ext}) are quantified to establish the baseline mechanical loads that the anchor must resist. Subsequently, the adhesive interface undergoes a two-stage validation: a parametric thermal screening to identify the optimal layer configuration for rapid switching, followed by rigorous normal and shear adhesion testing to verify that the cold-state adhesion strength exceeds the required magnetic loads. To address navigation constraints, the structural compliance of the robot is analysed using finite element simulation (COMSOL) and experimental verification, confirming its ability to deform under high-gradient fields. Finally, the integrated system is evaluated through functional demonstrations, including line formation, ring assembly, and collective rotation, to prove the efficacy of the selective control principle in a physical swarm.

3.3 Robot architecture and fabrication

This section describes how the robot and its operating surface were physically realised to satisfy the selective principles introduced in Section 3.2. The design combines a hexagonal TPU robot with an asymmetric three-magnet configuration and a separate EVA–foil–acrylic substrate. Fabrication implements this architecture through 3D printing, magnet embedding, and preparation of the EVA-coated surface.

3.3.1 Hexagonal geometry and face assignment

Each robot is a compact hexagonal prism with a flat-to-flat distance of 15 mm and a width of 5 mm. The regular hexagon was chosen because it tessellates the plane without gaps, offers six flat faces for reproducible magnet placement, and distributes mechanical stresses more uniformly than square or triangular alternatives. A comparison of candidate geometries (circle, square, triangle, hexagon) is provided in Appendix A.

Three faces (0, 2, and 4) contain shallow cavities (0.5 mm depth) for embedding N45SH magnets, which stiffen these sections into rigid links. The remaining faces (1, 3, and 5) are left unmagnetised. Semicircular relief grooves are located at the vertices between adjacent faces (visible in Fig. 8). These grooves reduce the local cross-sectional stiffness, effectively functioning as compliant flexures. When the robot is subjected to strong magnetic loading, these flexure points allow the structure to pinch inward in a controlled manner, while the magnetised faces remain relatively rigid due to the embedded magnets.

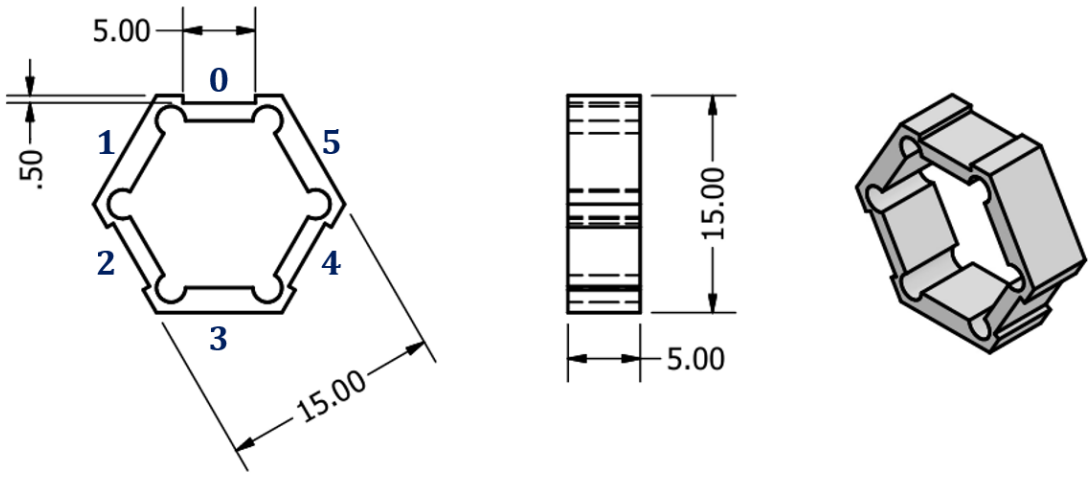

Figure 8: Technical drawing of the robot geometry. Cavities on faces 0, 2, and 4 house rigid magnets. Semicircular relief grooves at the vertices between faces act as compliant flexures to enable controlled pinching deformation.

3.3.2 Three-magnet configuration and net dipole moment

The magnetic configuration was designed to (i) generate a non-zero net dipole moment for rotation, (ii) enforce predictable face-to-face coupling for assembly, and (iii) keep robot–robot forces within the force hierarchy of Eq. (1).

N45SH block magnets (5 mm × 4 mm × 1 mm) were embedded in faces 0, 2, and 4, which are separated by 120°. The polarity assignment follows an asymmetric $(+,-,-)$ pattern:

$$s_0 = +1 \text{ (north pole outward)}, \qquad s_2 = s_4 = -1 \text{ (north poles inward)}. \tag{2}$$

Faces 1, 3, and 5 contain no magnets and therefore do not contribute directly to the dipole.

A uniformly magnetised body of volume V and magnetisation M behaves as a dipole with moment $\mathbf{m} = MV\hat{\mathbf{n}}$, where $\hat{\mathbf{n}}$ is the magnetisation direction. For the three-magnet robot, the net dipole moment is

$$\mathbf{m}_{\text{net}} = m_0 \sum_{i\in\{0,2,4\}} s_i\, \hat{\mathbf{n}}_i, \tag{3}$$

where m_0 is the dipole moment of a single magnet and $\hat{\mathbf{n}}_i$ is the outward normal of face i. Using the face normals of a regular hexagon and the polarity pattern in Eq. (2), the vector sum simplifies to (derivation in Appendix B):

$$\boxed{\mathbf{m}_{\text{net}} = 2m_0\,\hat{\mathbf{x}}.} \tag{4}$$

Thus, the robot has a resultant dipole of magnitude $2m_0$ pointing along face 0 (Fig. 9). This establishes a well-defined heading direction in uniform fields and a clear attraction/repulsion map between neighbouring robots.

Using the magnet properties in Table 1, the single-magnet moment is estimated as

$$m_0 = MV = \frac{B_r}{\mu_0}V \approx 2.15 \times 10^{-2}\ \text{A} \cdot \text{m}^2,$$

giving a net moment $|\mathbf{m}_{\text{net}}| \approx 4.3 \times 10^{-2}$ A·m^2 for each robot.

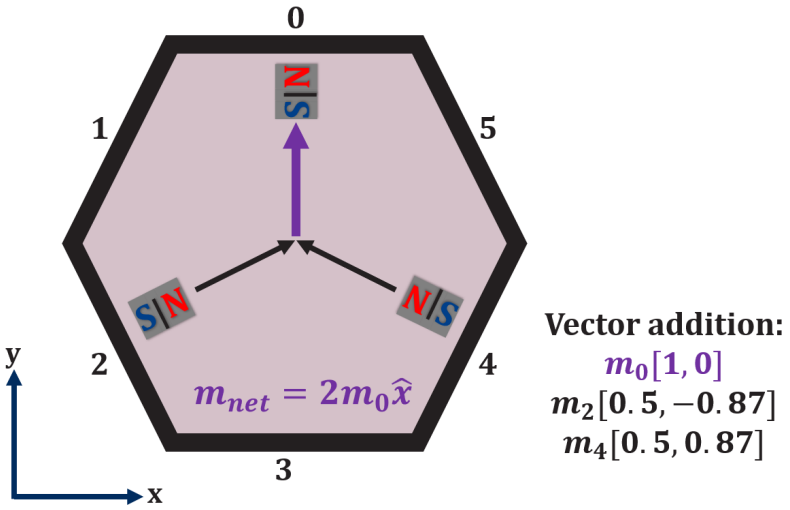

Figure 9: Three-magnet configuration and resulting net dipole. Face 0 has its north pole oriented outward, while faces 2 and 4 have north poles oriented inward. Vector addition of the individual dipole moments yields $\mathbf{m}_{\text{net}} = 2m_0\hat{\mathbf{x}}$ pointing along face 0.

Table 1: Magnetic properties used for dipole moment estimation.

Property	Symbol	Value	Unit
Magnet dimensions	—	$5 \times 4 \times 1$	mm
Volume	V	2.0×10^{-8}	m^3
Remanent flux density	B_r	1.35	T
Magnetisation	$M = B_r/\mu_0$	1.07×10^6	A/m

A more symmetric assignment with four or six magnets would increase the inter-robot forces F_{AB} and reduce the safety margin in Eq. (1). The chosen three-magnet layout provides a strong net dipole for control while keeping coupling forces within the adhesion limits.

3.3.3 Material selection

The material choices were made to satisfy the mechanical and thermal requirements imposed by the selective unlocking principle. Each selection was informed by preliminary experiments and by the need to balance structural integrity, compliance, adhesion behaviour, and compatibility with RF heating.

The robot body is printed in thermoplastic polyurethane (TPU, Shore 85A). TPU-85A provides enough stiffness to preserve the geometry of the hexagon and to keep the embedded magnets securely positioned, while still being flexible enough to deform when required. This deformability is a functional requirement of the system: the robot must be able to narrow or "pinch" its shape under magnetic loading in order to grasp, release, or guide small payloads, and to adapt when operating in confined spaces. As a result, the material must balance shape retention with reversible bending along the non-magnetised faces.

Stiffer materials such as PLA were rejected because they cannot tolerate bending. Softer silicone elastomers were also excluded because they do not hold the permanent magnets securely and showed poor contact behaviour with the EVA-coated substrate.

The reversible adhesive is provided by an EVA hot-melt layer applied to the substrate surface. EVA behaves as a rigid, high-strength adhesive at room temperature ($\approx$ 20–25°C) and softens above 80°C, where its cohesive strength drops to nearly zero. This temperature-dependent transition aligns with the force hierarchy in Eq. (1) and enables switching between locked and unlocked states during operation.

A thin aluminium foil is laminated beneath the EVA and serves as the RF-heating susceptor. Under the 125 kHz field of the RF coil, the foil heats locally, allowing a single region of the substrate to be activated without affecting the surrounding workspace. This localisation is key to enabling selective locking or unlocking of one robot while all neighbouring robots remain anchored. The specific EVA and foil thicknesses used in the final system correspond to the configuration identified in the thermal screening study presented later in Section 3.6.3.

3.3.4 Fabrication protocol

The fabrication process implements the robot architecture using standard 3D printing, manual magnet embedding, and preparation of the EVA–foil substrate. Relevant mechanical and thermal properties of TPU-85A, and the N45SH magnets are summarised in Appendix C.

Robot printing. Robots were printed on a Bambulab FDM printer using TPU-85A filament and the geometry defined in Fig. 8. Printing parameters were adjusted to ensure accurate cavity dimensions and reliable wall thicknesses.

Magnet embedding. After printing, the N45SH magnets were embedded in faces 0, 2, and 4 according to the $(+,-,-)$ polarity pattern defined in Eq. (2). Each magnet's north–south orientation was verified with a flux detector sheet prior to insertion. A small amount of cyanoacrylate adhesive was applied inside each cavity, and the magnets were pressed into place with a non-magnetic tool. A final polarity check confirmed correct orientation. No magnet displacement or rotation was observed during any of the thermal or actuation experiments (Fig. 10).

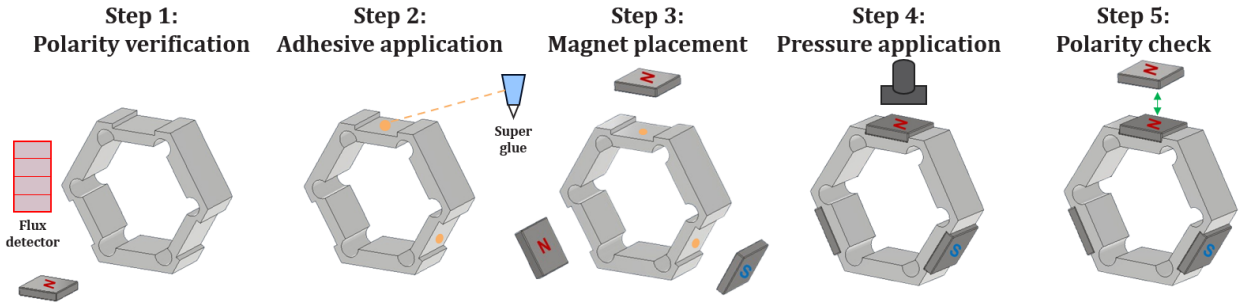

Figure 10: Magnet embedding procedure. Magnets are oriented using a flux detector sheet, placed into the cavities, and pressed into place before a final polarity check.

Adhesive interface preparation. The substrate used for all locking–unlocking and assembly experiments consists of an acrylic base, an aluminium susceptor layer, and an EVA adhesive layer (Fig. 11). Aluminium foil squares (1 cm $\times$ 1 cm) were first glued onto the acrylic sheet to define discrete heating zones.

The EVA sheet was prepared separately. EVA glue sticks were placed onto a flat metal plate positioned on a laboratory hotplate magnetic stirrer. As the plate was heated, the EVA softened uniformly and was spread using calibrated 1 mm spacers to obtain a controlled thickness of approximately 1.0 mm *(the choice of a 1 mm EVA layer is justified later through the thermal parameter study; see Section 3.6.3)*. After cooling, the EVA sheet was peeled cleanly from the metal surface and transferred onto the foil-patterned acrylic. Gentle reheating with a hot-air gun ensured proper bonding between EVA and foil without excessive melting or surface unevenness.

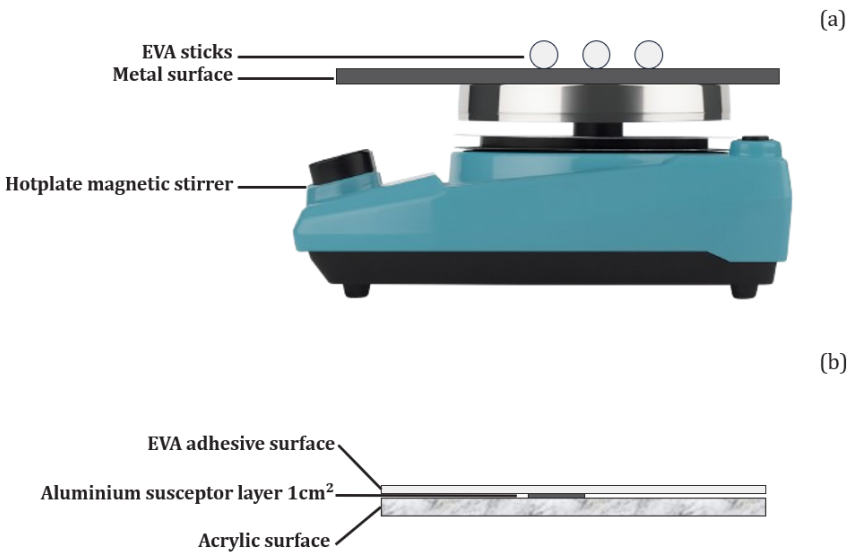

Figure 11: Fabrication of the adhesive interface. (a) EVA preparation: Commercial adhesive sticks are melted on a controlled hotplate to form a uniform sheet. (b) Cross-sectional schematic of the final substrate stack, showing the acrylic base, the 1 cm^2 aluminium susceptor for RF heating, and the top EVA adhesive layer.

In the cold state, the EVA surface provides a strong adhesive bond that withstands the magnetic interaction forces between neighbouring robots. After local RF heating, the same region softens and allows the robot to detach under the available magnetic forces, satisfying the requirements of Eq. (1).

3.4 Single-robot capabilities

Before examining how multiple robots interact to form assemblies, it is necessary to establish what an individual robot can do under magnetic actuation. The net dipole moment $\mathbf{m}_{\text{net}} = 2m_0\hat{\mathbf{x}}$ derived in Eq. (4) determines the robot's response to external magnetic fields. This section describes the fundamental single-robot behaviours: rotation, translation, and deformation, that serve as building blocks for the collective behaviours.

3.4.1 Magnetic actuation: rotation and translation

Under a spatially uniform magnetic field $\mathbf{B}_{\text{ext}}$, the robot experiences a magnetic torque given by

$$\boldsymbol{\tau} = \mathbf{m}_{\text{net}} \times \mathbf{B}_{\text{ext}}. \tag{5}$$

This torque tends to align the robot's dipole axis with the field direction. If the field rotates in the plane (as produced by a Helmholtz coil), the robot tracks the field orientation, enabling controlled in-plane rotation (Fig. 12a).

To verify the rotational capability under controlled conditions, a single robot was placed inside a Helmholtz coil workspace and subjected to a uniform rotating field. The robot was observed to rotate synchronously

with the applied field at frequencies between 0.05 and 0.2 Hz and field magnitudes of 1–2 mT. This establishes the basic rotational response of the robot under uniform fields and demonstrates that the net dipole moment $\mathbf{m}_{\text{net}}$ is sufficient to overcome substrate friction and produce controlled rotation. Representative experimental sequences of single-robot rotation are presented in Section 4.5.

In addition to torque, a spatially non-uniform (gradient) field exerts a translational force on the magnetic dipole:

$$\mathbf{F}_{\text{mag}} = \nabla(\mathbf{m}_{\text{net}} \cdot \mathbf{B}_{\text{ext}}). \tag{6}$$

This gradient force enables directed locomotion (Fig. 12b). By positioning an external gradient magnet beneath the EVA-coated substrate and moving it laterally, the robot can be steered in any in-plane direction. The translational speed is limited primarily by the adhesion and friction forces between the robot and the EVA surface. While the gradient field source can occasionally induce rotation through manual manipulation, this rotational control is limited and not reliably repeatable. Consequently, all demonstration experiments involving locking, unlocking, line formation, and ring assembly (Section 3.8) rely primarily on gradient-field translation rather than uniform-field rotation, as the Helmholtz coil and the EVA/RF heating platform are located in different laboratory facilities and cannot be operated simultaneously.

3.4.2 Mechanical deformation under magnetic loading

The TPU-85A body, with its Shore hardness of 85A, is sufficiently compliant to deform reversibly under strong magnetic loading. As described in Section 3.3.1, the semicircular relief grooves at the vertices act as compliant flexures, allowing the robot to pinch inward when subjected to concentrated forces (Fig. 12c). Under particularly strong loading such as when strong gradient fields are applied, the structure exhibits a pinching mode in which the compliant flexure points at the vertices bend inward, while the faces themselves remain relatively straight. The embedded magnets provide local stiffening to faces 0, 2, and 4. This deformation is driven primarily by the two bottom magnets (faces 2 and 4, north poles inward), which experience forces from the vertical field gradient that compress the robot.

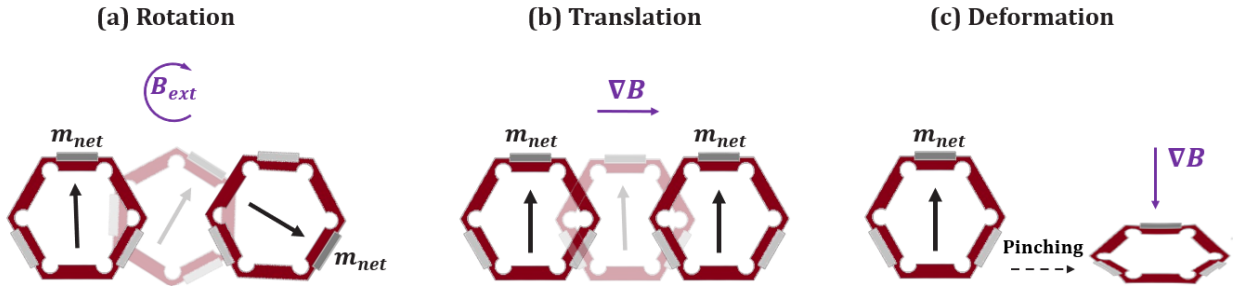

Figure 12: Schematic illustration of single-robot capabilities. (a) Rotation under uniform rotating field $\mathbf{B}_{\text{ext}}$ via magnetic torque. (b) Translation under gradient field $\nabla\mathbf{B}$ via magnetic force. (c) Deformation under strong gradient field $\nabla\mathbf{B}$: the two bottom magnets (faces 2 and 4, north poles inward) experience forces that cause vertical compression and pinching at the compliant flexure points.

3.4.3 Adhesion interface behaviour

The interaction between the TPU robot and the EVA substrate switches between two discrete mechanical states depending on temperature. In the cold state (room temperature, approximately 20–25°C), the EVA is rigid and exerts a strong adhesion force $F_{\text{adh,cold}}$ that effectively anchors the robot to the substrate. This anchoring force must exceed both the robot–robot magnetic coupling force and the external pulling force, as required by the force hierarchy in Eq. (1).

In the hot state (above 80°C), the EVA softens and the adhesion drops to near-zero ($F_{\text{adh,hot}} \approx 0$). The softened interface allows the robot to be detached easily under the same magnetic forces that were insufficient to overcome the cold-state adhesion. This transition is what enables selective actuation: by locally heating a specific zone of the substrate, a single robot can be unlocked and repositioned while all neighbouring robots are firmly anchored on cold EVA.

Quantitative measurements of the cold-state and hot-state adhesion forces are presented in Section 4.3, where it is shown that the cold-state adhesion provides a sufficient safety margin above the maximum magnetic forces measured in Section 4.1. Together, these single-robot capabilities (rotation, translation, deformation, and thermally switchable adhesion) form the foundation for the multi-robot collective behaviours described in Section 3.5.

3.5 Collective behaviour: lines and rings

Building on the single-robot capabilities described in Section 3.4, we now examine how multiple robots interact magnetically to form stable assemblies. The net dipole moment $\mathbf{m}_{\text{net}} = 2m_0\hat{\mathbf{x}}$ derived in Eq. (4) not only determines individual robot behaviour but also dictates how robots self-assemble through magnetic coupling. This section describes two primary collective structures enabled by the asymmetric three-magnet configuration: head-to-tail lines and closed rings.

3.5.1 Line formation

When robots are aligned head-to-tail, their net dipoles become collinear and attract in a preferred orientation. This produces stable magnetic chains in which interior robots experience balanced neighbour forces (Fig. 13). For an N-robot line, the individual dipole moments sum vectorially to produce a total dipole:

$$\mathbf{m}_{\text{line}} = N \cdot \mathbf{m}_{\text{net}} = 2Nm_0\hat{\mathbf{x}}. \tag{7}$$

This linear scaling means that longer chains possess proportionally stronger net dipoles. Under a uniform rotating field (as demonstrated separately in the Helmholtz coil; see Section 3.4.1), such a line would rotate as a rigid assembly, tracking the external field direction. However, the increased dipole magnitude also means that higher field strengths are required to overcome the greater friction force from the longer assembly and heavier cumulative mass.

In the context of the force hierarchy in Eq. (1), the magnetic coupling between neighbouring robots in the line must be strong enough for the chain to move as a unit during gradient-field translation, yet remain weaker than the cold-state adhesion so that anchored robots do not detach unintentionally during assembly or manipulation.

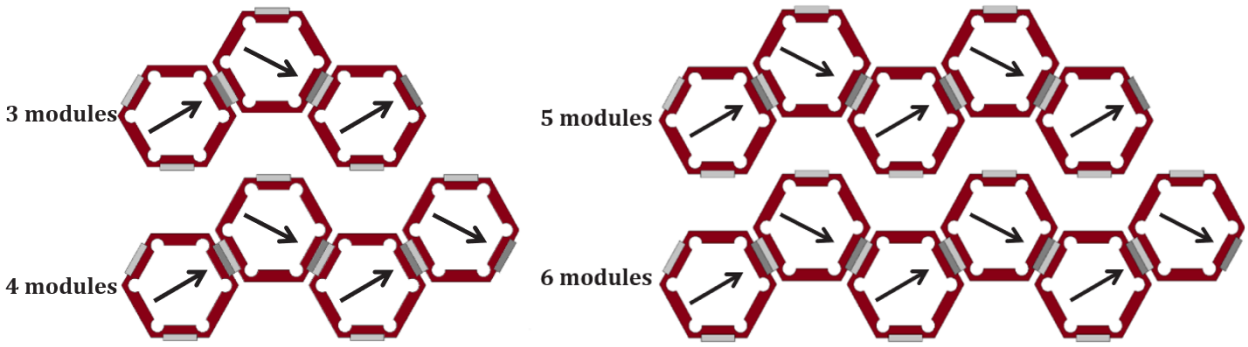

Figure 13: Head-to-tail line formation for multiple robots. Each robot's net dipole aligns along the chain axis, producing a stable magnetic structure with a cumulative dipole moment of $\mathbf{m}_{\text{line}} = 2Nm_0\hat{\mathbf{x}}$.

3.5.2 Ring formation

When robots are arranged on a circular path with tangentially oriented dipoles, attraction between neighbours produces a mechanically stable ring. In the nominal case where all robots have identical polarity patterns, the individual dipole moments are equally spaced around the ring and their vector sum cancels:

$$\sum_{i=1}^{N} \mathbf{m}_{\text{net},i} \approx \mathbf{0}. \tag{8}$$

As a result, the structure has no net dipole. For a symmetric ring with zero net dipole, the magnetic torque (Eq. 5) vanishes and the assembly does not exhibit rigid-body rotation under a uniform field (Fig. 14a).

However, the ring can still be translated as a whole under a gradient magnetic field. Although the net dipole is zero, each individual robot experiences a position-dependent force $\mathbf{F}_i = \nabla(\mathbf{m}_i \cdot \mathbf{B})$. The non-uniform spatial distribution of the gradient field means that robots closer to the field source experience stronger forces than those farther away, producing a net translational force on the assembly. This allows gradient-field manipulation of rings even when they cannot rotate under uniform fields.

To enable rotation under uniform fields, one robot in the ring must be intentionally reversed where its polarity assignment becomes $(s_0, s_2, s_4) = (-1, +1, +1)$ instead of the standard $(+1, -1, -1)$ pattern. This reversal inverts the robot's net dipole:

$$\mathbf{m}_{\text{net,reversed}} = -2m_0\hat{\mathbf{x}}. \tag{9}$$

The reversed robot breaks the symmetry of the ring and introduces a non-zero global dipole (Fig. 14b). For a ring of N robots with one reversed, the net dipole becomes:

$$\sum_{i=1}^{N} \mathbf{m}_{\text{net},i} = (N-1)(2m_0) - 2m_0 = 2m_0(N-2). \tag{10}$$

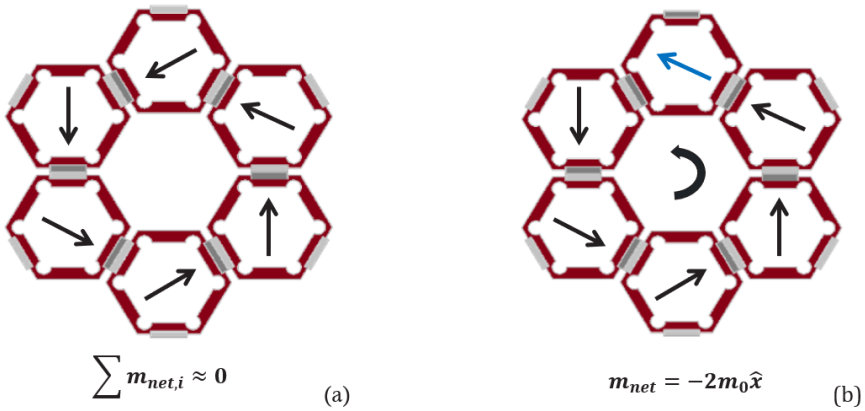

Figure 14: Dipole behaviour in six-robot rings. (a) Nominal ring with tangential dipoles that cancel globally, giving a net-zero moment. (b) Ring with one reversed-polarity robot (polarity pattern $(-1, +1, +1)$ instead of $(+1, -1, -1)$), introducing a non-zero global dipole that enables collective rotation under a uniform rotating field.

Experimentally, rings were observed to rotate in the Helmholtz coil at field magnitudes that scale with ring size and net dipole strength. A five-robot ring (net dipole $6m_0$) rotated stably at fields above 10 mT, while six-robot and seven-robot rings required slightly higher fields (12–18 mT) due to their increased mass and friction. The reversed robot must be positioned at the top of the assembly (aligned with the initial field direction) to maximize rotational stability. If positioned elsewhere in the ring, the asymmetric mass distribution and uneven friction forces lead to increased wobble as the assembly rotates.

As ring size increases beyond six or seven robots, mechanical stability decreases despite the stronger net dipole. Each robot contributes 5 mm of width and 15 mm of height, so larger rings become progressively heavier. The cumulative mass increases friction and inertia, while the larger circumference introduces potential for non-uniform contact with the surface and out-of-plane buckling. This limits practical ring sizes to approximately five to seven robots under the available field strengths (up to 50 mT from the Helmholtz coil).

3.6 Experimental characterisation

This section describes how the mechanical and thermal quantities in the force hierarchy of Eq. (1) were measured or estimated. The goal is to obtain quantitative values for the robot–robot magnetic coupling

force F_{AB}, the external actuation force F_{ext}, the cold- and hot-state adhesion forces ($F_{\text{adh,cold}}$, $F_{\text{adh,hot}}$), and the heating and cooling times (t_{80}, t_{cool}). In parallel, finite-element simulations were used to extend the analysis to magnetic field strengths and deformation aspects that are difficult to access experimentally.

3.6.1 Magnetic actuation systems

All experiments rely on two magnetic actuation sources (Fig. 15). A handheld cylindrical N45 permanent magnet (35 mm diameter × 20 mm height) provides strong gradient fields used for robot translation, selective detachment, and force-distance measurements. This magnet produces the external pulling force F_{ext} that appears in the force hierarchy.

A three-axis PacMag Helmholtz coil system generates spatially uniform magnetic fields up to 50 mT, which are used for controlled rotation experiments and deformation analysis under well-defined field conditions.

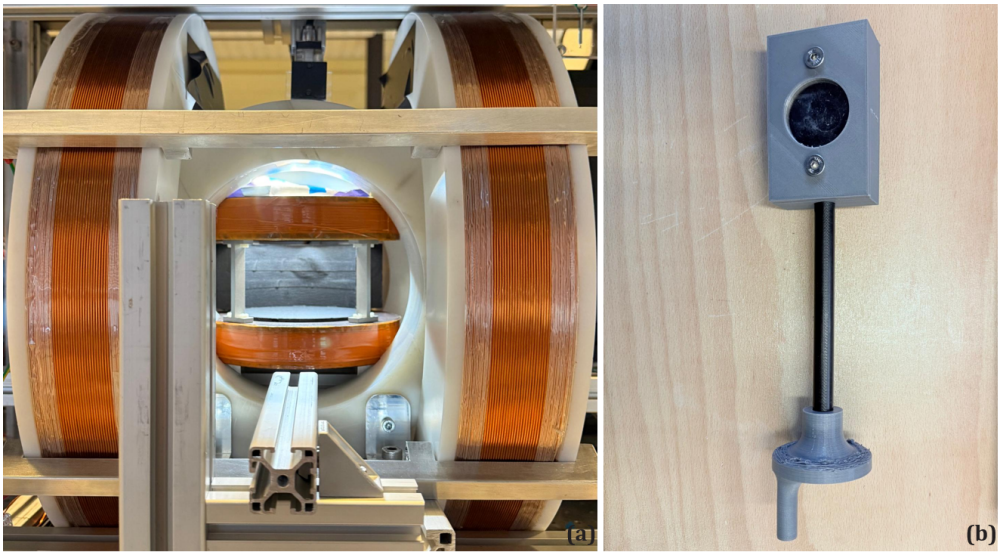

Figure 15: Magnetic actuation systems used throughout the study. (a) PacMag Helmholtz coil for uniform magnetic fields up to 50 mT. (b) Handheld N45 cylindrical magnet for gradient-field actuation.

3.6.2 Magnetic force measurement

Magnetic interaction forces were measured to determine the mechanical loads that the EVA anchor must resist during operation. These measurements provide the values of the robot–robot coupling force F_{AB} and the external pulling force F_{ext}, both of which form the upper bounds in the force hierarchy of Eq. (1). During assembly, robots experience rapidly increasing attraction at small gaps, transmitting contact forces through the EVA interface. During selective detachment, the external magnet applies a pulling force that must remain below the cold-state adhesion for proper function.

Magnetic forces were measured using a K3D40 triaxial force sensor (±10 N per axis) mounted on a non-magnetic acrylic base. A 3D-printed stand held a single N45SH block magnet (representing one robot face). The interacting component (either another block magnet or the cylindrical actuation magnet) was mounted on a calibrated Z-stage to vary the separation distance with millimetre accuracy (Fig. 16). Full sensor specifications, mounting details, and calibration parameters are provided in Appendix D.

Two interaction types were tested. The first measured the force between two robots, which represents both the contact force during assembly and the steady coupling force that maintains lines and rings. The second measured the interaction between a robot and the external actuation magnet, which determines the forces available for locomotion and peeling during unlocking.

For each test, the vertical gap r was swept between 0 mm to 70 mm. At every distance, the normal force F_z was sampled at 10 Hz and averaged over 50 readings. Each sweep was repeated five times to

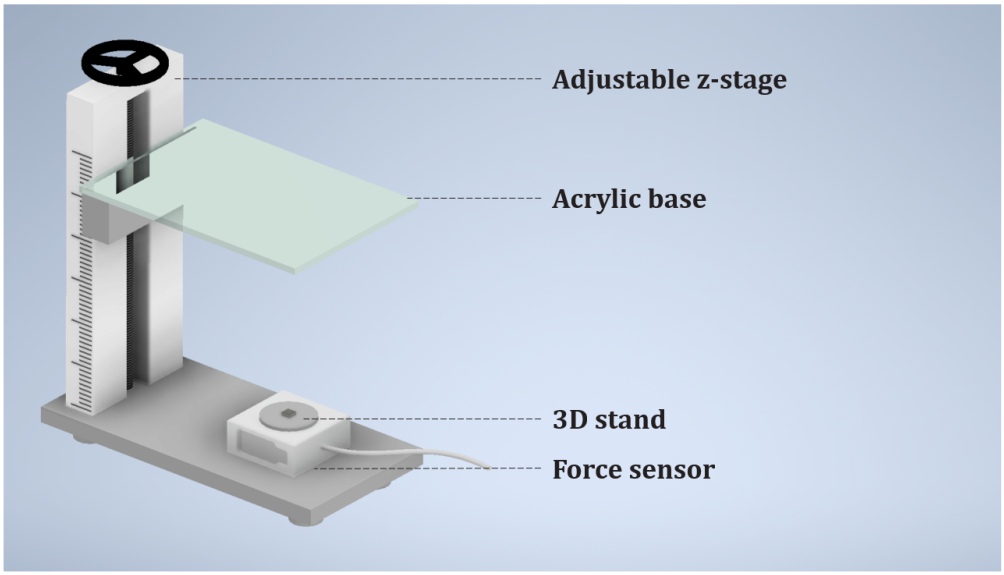

Figure 16: Setup for magnetic force measurements. The lower magnet is fixed to the triaxial force sensor, and the upper component is positioned using a Z-stage to control the separation distance.

ensure repeatability. The resulting force–distance curves were processed in Python and later compared with finite-element predictions in Section 3.7. Together, these measurements provide the quantitative basis for assessing the force hierarchy in Chapter 4 and for validating whether the EVA interface can anchor the robots throughout assembly, locomotion, and selective detachment.

3.6.3 Thermal activation screening

The thermal activation test evaluates whether the EVA–foil substrate can switch between a strongly adhesive state and a softened state that allows a robot to detach. In terms of the force hierarchy in Eq. (1), it provides the two quantities needed for selective unlocking: the heating time required to reach the softening point of EVA (t_{80}) and the cooling time needed for the interface to regain adhesion (t_{cool}). Because the adhesive behaviour depends directly on how heat travels through the EVA and how efficiently the aluminium foil acts as a susceptor, this experiment also determines which combination of EVA thickness, aluminium thickness, and coil distance can produce a practical and repeatable switching response.

RF induction heating was used because it allows heat to be applied to a single location on the substrate without affecting the surrounding area, which is essential when only one robot should unlock while neighbouring robots remain fixed. A 125 kHz induction heater generated eddy currents in the aluminium foil layer beneath the EVA. The coil was positioned below a 2 mm acrylic plate on an adjustable z-stage to vary the coil–foil distance between 1 and 5 cm (Fig. 17). Surface temperature was monitored with a Fluke Ti400 infrared camera. A hot-air nozzle was only used in early checks to verify that EVA softens between 80–85°C; all systematic measurements were performed with the RF system.

The EVA–foil samples were made from the same materials as the final substrate, but with different combinations of layer thicknesses. EVA sheets were prepared by melting commercial hot-melt sticks on a metal plate and spreading the melt using calibrated spacers to obtain thicknesses of 0.5, 1.0, or 2.0 mm. Aluminium heating patches (1 cm × 1 cm) were prepared in three effective thicknesses: 16 µm, 48 µm, and 100 µm. These two parameters were varied because thicker EVA slows down heating, while thicker aluminium absorbs more RF energy; the goal was to find a practical balance that allows fast heating without overheating the substrate.

A full-factorial screening study was carried out to determine how EVA thickness, foil thickness, and coil distance influence the heating behaviour. The tested levels were $h_{\text{EVA}} = 0.5, 1.0, 2.0$ mm, $h_{\text{Al}} = 16, 48, 100$ µm, and $d = 1, 2, 3, 5$ cm, resulting in 36 total combinations. For each sample, the RF coil was switched on until the EVA reached $T \approx 80$°C and then allowed to cool passively to below 40°C. From

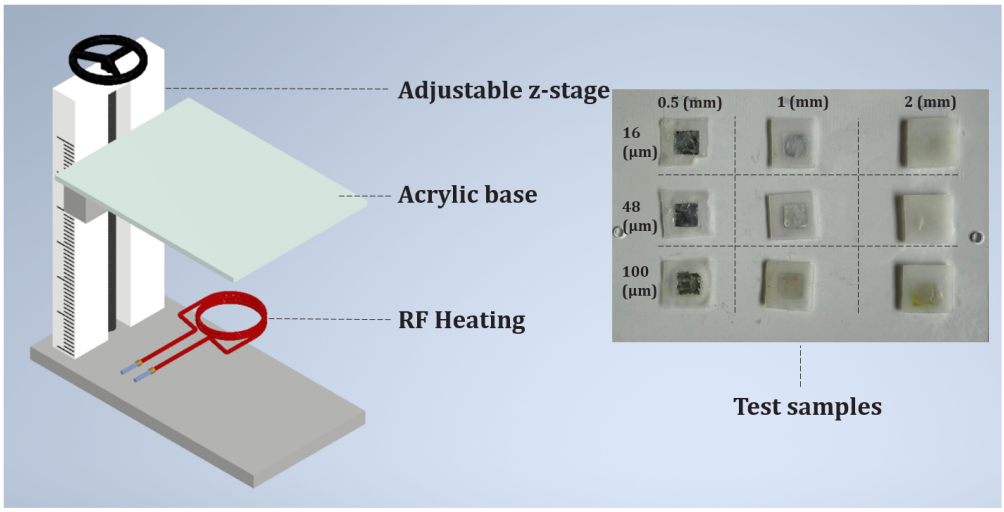

Figure 17: Thermal screening setup. The RF induction coil is positioned below a 2 mm acrylic plate. EVA sheets with aluminium-foil heating patches were tested at different coil distances.

the temperature–time curves, t_{80}, t_{cool}, and the peak temperature were extracted. A baseline case (1.0 mm EVA, 48 µm foil, 1 cm distance) was repeated five times to check repeatability. All temperature data are reported in Appendix E.

The screening identified the configuration of 1.0 mm EVA on 48 µm aluminium at a coil distance of 1 cm as the most suitable for the system requirements. This combination was selected based on four criteria: (1) heating time $t_{80} < 60$ s, (2) no thermal overshoot above 100°C, (3) no robot sinking into the softened EVA, and (4) repeatable geometric stability across multiple heating–cooling cycles. Alternative configurations failed to satisfy one or more of these constraints. The selected configuration was used for all subsequent adhesion tests and demonstration experiments, and the detailed screening outcomes are presented in Section 4.2.

3.6.4 Adhesion strength testing

After establishing the magnetic forces in the system, the next step was to determine whether the EVA interface can anchor a robot strongly enough to satisfy the force hierarchy in Eq. (1). In the cold state, the adhesion must exceed both the robot–robot coupling force and the external pulling force ($F_{\text{adh,cold}} > F_{AB}, F_{\text{ext}}$). In the hot state, adhesion must fall to a negligible level so that the same magnetic forces are sufficient to detach the robot. The purpose of this experiment is therefore to quantify the cold-state adhesion strength and verify that it lies above the magnetic loads measured in Section 3.6.2.

Cold-state adhesion was measured using an Instron universal testing machine (1 kN load cell) fitted with custom 3D-printed fixtures (Fig. 18). Each specimen consisted of a TPU robot bonded to a 1.0 mm EVA layer on top of a 48 µm aluminium-foil/acrylic substrate (the same configuration selected from the thermal screening study). To replicate realistic operation, the EVA was softened using the RF coil (Section 3.6.3), and the robot was pressed into the heated adhesive with the external gradient magnet before being allowed to cool.

Two loading modes were tested to capture the main mechanical actions relevant to operation. In the normal (out-of-plane) adhesion test, the substrate was mounted horizontally and the robot was pulled perpendicular to the surface at 20 mm/min until detachment. This loading case represents the way the external magnet eventually pulls and peels the robot away from the EVA during unlocking. In the shear (in-plane) adhesion test, the substrate was mounted vertically and a horizontal tensile load was applied at 20 mm/min. This test captures the lateral sliding forces that occur when robots bump into each other during magnetic assembly or are dragged slightly along the surface while still locked.

In both tests, a 3D-printed fixture's shaft was positioned at the geometric centre of the robot to ensure symmetric loading. Force–displacement data were recorded at 10 Hz until complete detachment, and three

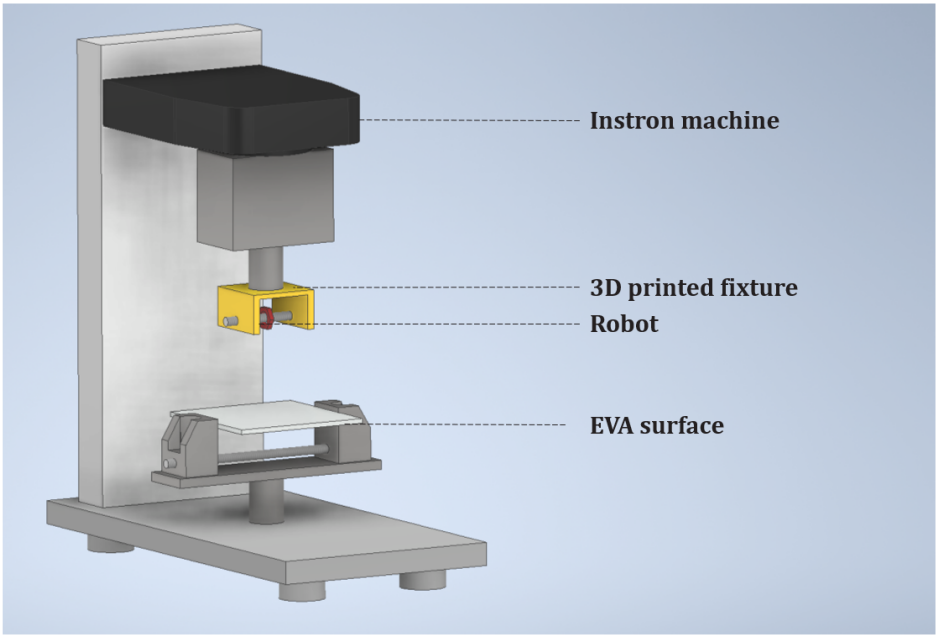

Figure 18: Instron test configuration for cold-state adhesion measurements. The robot is bonded to the EVA–foil surface and pulled either vertically (normal) or laterally (shear) using dedicated fixtures.

specimens were tested for each loading mode. These measurements provide the values of $F_{\mathrm{adh,cold}}$ used later in Chapter 4 to evaluate whether the EVA interface provides sufficient margin above the magnetic forces characterised earlier.

3.7 COMSOL simulations

Finite-element simulations were used to complement the experimental characterisation and to explore conditions that cannot be reproduced with the available hardware. The PacMag Helmholtz coil provides uniform magnetic fields up to 50 mT, which is sufficient for rotation experiments but not for inducing the large deformations and pinching behaviour observed when robots are actuated with strong gradient fields. COMSOL therefore provides a controlled way to study both magnetic forces and deformation across a wider field range (10–500 mT).

The simulations also serve a second purpose: once the magnetic force predictions are validated against the experimental force–distance measurements, the same model can be used to evaluate future design variations without needing to fabricate and test each one physically.

3.7.1 Simulation objectives

Two classes of quantities were evaluated. First, magnetic interaction forces were predicted as functions of separation distance for robot–robot coupling and robot–external-magnet actuation. These curves are compared directly with the experimental data from Section 3.6.2. Second, robot deformation was analysed to understand how a single robot and a six-robot ring deform when exposed to uniform magnetic fields.

The deformation simulations are motivated by potential applications: a single robot must be able to compress to pass through restricted anatomical regions or deliver a payload, and a ring of robots should be able to pinch inward to grip an object. Since these deformations require field strengths well above the 50 mT coil limit, COMSOL was used to map the relationship between field magnitude and achievable shape change.

3.7.2 Model setup

Four configurations were simulated: (i) robot–robot magnetic force vs. gap, (ii) robot–external-magnet force vs. gap, (iii) single-robot deformation under uniform field, and (iv) six-robot ring deformation.

Magnetic force simulations were carried out in 3D domains, with air regions extending at least ten times the magnet size (Fig. 20). The embedded magnets were modelled with their real dimensions (5 mm × 4 mm × 1 mm), and the external actuation magnet was modelled as a 35 mm diameter × 20 mm height cylinder. For deformation studies, 2D planar geometries were used under a plane-stress assumption (Fig. 19). The CAD models of the hexagon and the six-robot ring were imported directly, with magnets assigned the same $(+,-,-)$ configuration as in the physical robots.

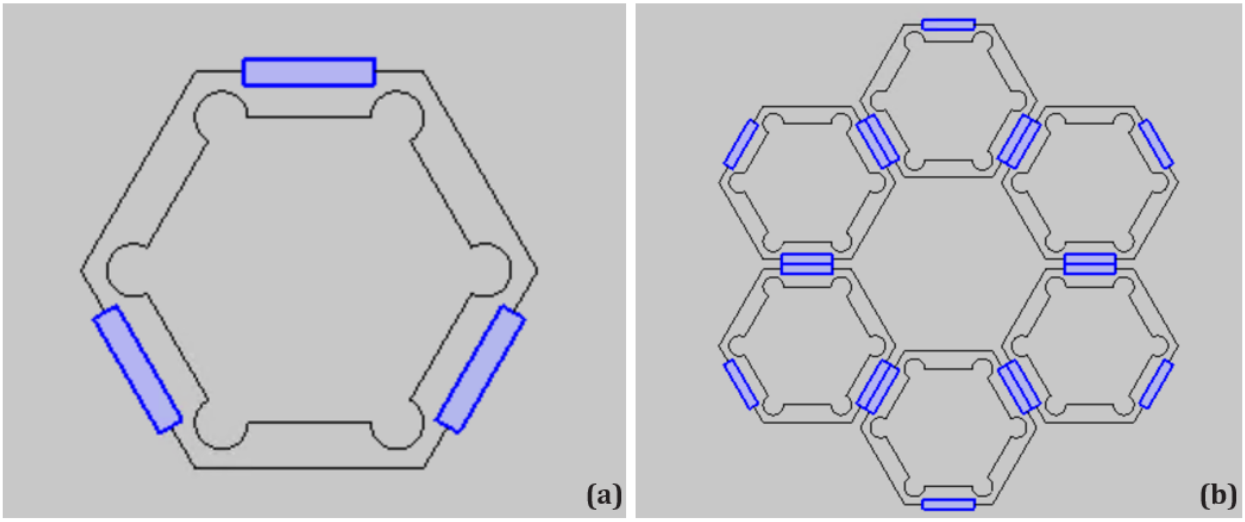

Figure 19: Planar geometries for deformation studies. (a) Single hexagonal robot with the $(+,-,-)$ magnet configuration. (b) Six-robot ring used to analyse deformation under uniform magnetic fields.

Magnetic interactions were modelled using the *Magnetic Fields, No Currents* interface:

$$\nabla \times \mathbf{H} = 0, \qquad \nabla \cdot \mathbf{B} = 0, \qquad \mathbf{B} = \mu_0 \mu_r \mathbf{H} + \mathbf{B}_r,$$

where $\mathbf{B}_r$ is the remanent flux of each magnet. For deformation simulations, this magnetic model was coupled to the Solid Mechanics interface. A small constraint was applied at one corner of the robot or ring to prevent rigid-body drift while still allowing free deformation. Uniform magnetic fields were applied along the global $+y$ direction to match the experimental coil orientation. Material parameters are listed in Table 2.

Table 2: Material properties used in COMSOL simulations.

Property	**TPU-85A**	**NdFeB (N45SH)**	**Air**
Relative permeability μ_r	1.00	1.05	1.00
Remanent flux density B_r	—	1.35 T	—
Young's modulus E	12 MPa	—	—
Poisson's ratio ν	0.49	—	—
Density ρ	1200 $\mathrm{kg\,m^{-3}}$	7500 $\mathrm{kg\,m^{-3}}$	1.2 $\mathrm{kg\,m^{-3}}$

All models were solved as stationary parametric sweeps. For magnetic force calculations, the gap distance was varied: 0–50 mm for robot–robot interactions, and 1–70 mm for robot–external-magnet interactions. For deformation studies, the applied uniform field magnitude B_0 was swept from 10 to 500 mT in increments of 10–50 mT depending on the convergence behaviour at each field level. Magnetic forces were extracted using the `Force Calculation` feature in COMSOL, and deformation metrics (displacement, von Mises stress, strain) were extracted directly from the solution nodes.

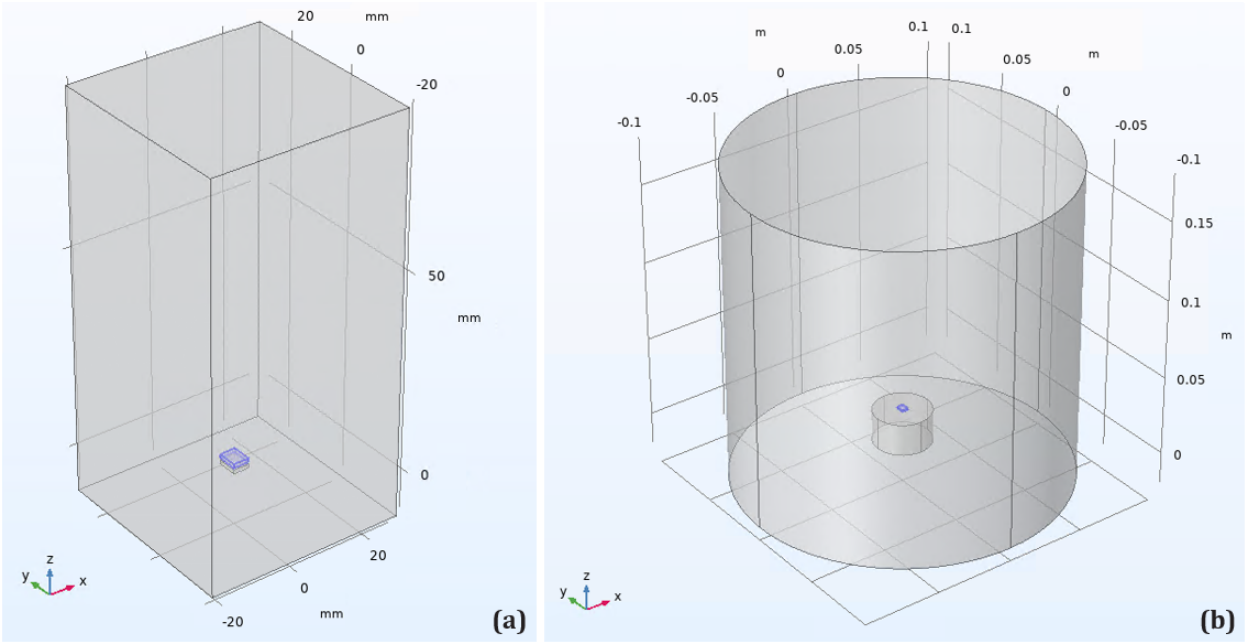

Figure 20: 3D air domains for magnetic force simulations. (a) Robot–robot configuration. (b) Robot–external-magnet configuration.

3.7.3 Validation approach

The force predictions from COMSOL were validated against experimental measurements (presented in Section 4.1). The robot–robot and robot–external-magnet force–distance curves were compared with the five repeated experimental sweeps described in Section 3.6.2.

The deformation predictions were not validated experimentally. The PacMag Helmholtz coil provides uniform fields up to 50 mT, which was insufficient to induce visible deformation in the TPU robots during controlled experiments. Qualitative observations with strong gradient fields from the external magnet confirmed that robots do deform under strong magnetic loading, exhibiting pinching behaviour. However, the non-uniform gradient field profile cannot be quantitatively compared to the uniform-field conditions used in the COMSOL deformation simulations. The deformation results from COMSOL (100–500 mT range) therefore remain model predictions without experimental validation at those specific field strengths.

3.8 Proof-of-concept demonstration experiments

The final stage of the methodology validated the selective control principle by combining magnetic actuation with local thermal activation in multi-robot scenarios. These tests confirm that the force hierarchy holds during realistic interactions and that robots can be selectively released without disturbing neighbouring robots.

As noted in Section 3.4.1, while single-robot rotation was verified separately using the PacMag Helmholtz coil, the demonstration experiments described below rely exclusively on gradient-field translation and manipulation. This is because the Helmholtz coil and the EVA substrate with RF heating are located in different laboratory facilities and cannot be operated simultaneously. For controlled, repeatable rotational studies (particularly for multi-robot ring assemblies) the Helmholtz coil was used separately without the thermal activation substrate (results presented in Section 4.5).

3.8.1 Experimental platform

All demonstrations were performed on a transparent acrylic platform (Fig. 21). Robots operated on the EVA–foil substrate on the upper surface, while the external cylindrical magnet (for locomotion and manipulation)

and RF coil (for heating) were positioned underneath. This arrangement allows independent control of motion and anchoring.

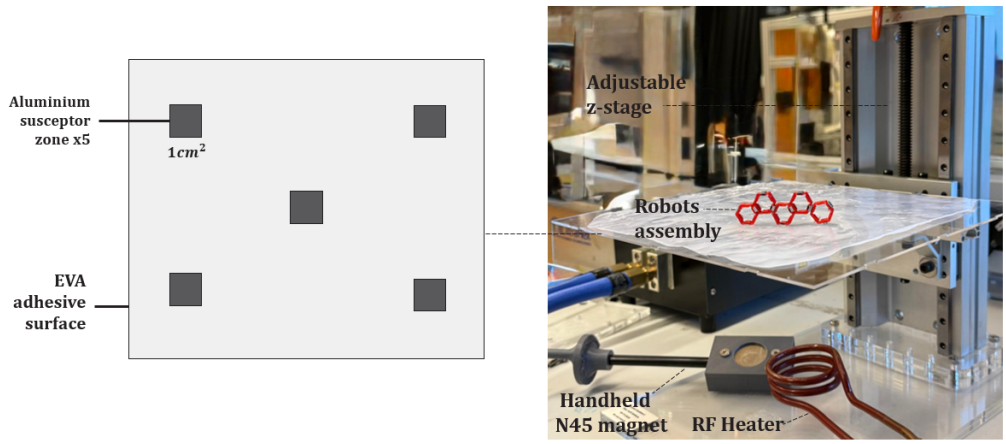

Figure 21: Experimental platform for demonstration experiments. Robots move on the EVA-coated top surface. The external magnet and RF coil are positioned below the acrylic sheet, enabling independent actuation and heating.

3.8.2 Demonstration protocols

Three proof-of-concept experiments were conducted, each repeated multiple times to assess repeatability.

Demonstration 1: Two-robot locking and unlocking. A heating spot was activated to soften the EVA. Robot A was then magnetically guided to the heated region using the external gradient magnet and allowed to cool, anchoring it to the substrate. Robot B was subsequently guided to Robot A and magnetically locked to it. While Robot A remained anchored, Robot B was magnetically manipulated to apply representative loads on the interface. Robot B was then magnetically peeled away from Robot A and moved to a different location. Finally, the anchoring spot beneath Robot A was reheated, allowing Robot A to be magnetically released and relocated. This test confirms that cold-state adhesion withstands neighbour manipulation and that individual robots can be selectively released on demand.

Demonstration 2: Selective assembly: line and ring formation. Robots were assembled into linear chains and five-robot rings by guiding them to dock with an anchored robot. The anchored robot resists the magnetic snap-in forces of incoming robots, confirming that $F_{\text{adh,cold}}$ exceeds the coupling forces measured in Section 3.6.2. Local reheating beneath a selected robot allowed detachment without disturbing the rest of the assembly.

Demonstration 3: Collective rotation under uniform fields. Rings of five, six, and seven robots were assembled with one polarity-reversed robot to generate a net dipole. The rings were placed inside the Helmholtz coil and actuated with a rotating uniform field at magnitudes ranging from 10 to 18 mT (depending on ring size) and frequencies of 0.05–0.2 Hz (Fig. 22). Coherent rigid-body rotation was observed, confirming the polarity-induced symmetry breaking described in Section 3.5.2.

All demonstrations were recorded using a fixed overhead camera and an eye-level camera. The corresponding motion sequences and quantitative outcomes are presented in Chapter 4.

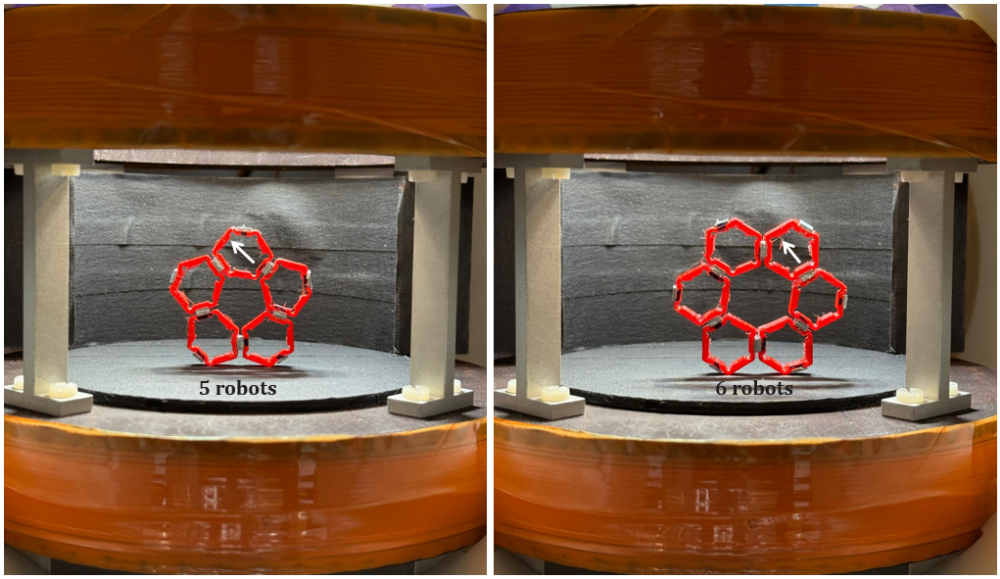

Figure 22: Ring rotation under a uniform rotating magnetic field. One robot is polarity-reversed to introduce a net dipole moment (white arrow), enabling coherent rotation of the multi-robot ring.

4 Results

4.1 Magnetic force characterisation

This section presents the measured magnetic interaction forces and compares them with the COMSOL simulations introduced in Section 3.7. Two interaction types were evaluated: (i) robot–robot magnetic coupling, and (ii) robot–external-magnet actuation forces. For each case, five repeated distance sweeps were performed following the protocol in Section 3.6.2, and the resulting $F_z(r)$ curves were analysed for repeatability and compared with finite-element predictions.

4.1.1 Repeatability of force–distance measurements

Figure 23 summarises the robot–robot interaction measurements across five repeated sweeps. The individual curves (top row) show a strongly nonlinear attraction profile, with a peak force of approximately -3.5 N at near-contact and a rapid decay over the first millimetres. In the zoomed regions (0–5 mm and 0–2 mm), the curves almost overlap, with only minor deviations at the smallest gaps.

The bottom-left panel shows the mean curve with shaded ± 1 standard deviation. The variance remains low across the full range, particularly for $r < 10$ mm, which corresponds to the operational magnetic-coupling range for the robots during assembly and line/ring formation. These results confirm that the measurement setup produces highly repeatable robot–robot force profiles.

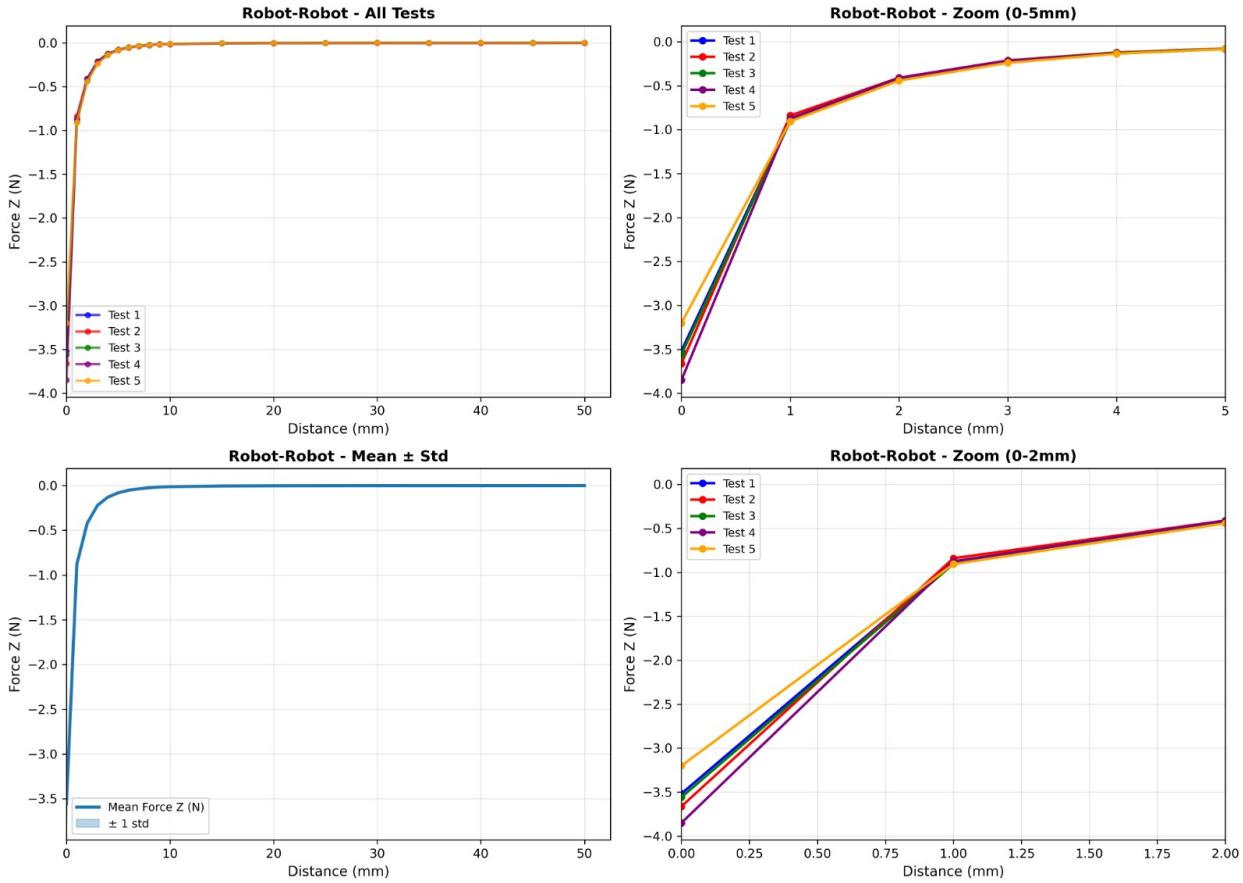

Figure 23: Robot–robot magnetic interaction forces across five repeated trials. Top: individual $F_z(r)$ curves for all five tests (left) and zoomed view for 0–5 mm (right). Bottom: mean force curve with shaded ± 1 standard deviation (left) and zoomed view for 0–2 mm (right). Peak force at near-contact: -3.5 ± 0.1 N. The tight grouping demonstrates high repeatability, especially in the sub-10 mm range relevant for inter-robot coupling.

Figure 24 shows the equivalent measurements for the robot–external-magnet interaction. The near-contact force is lower (approximately −1.2 N), but the decay with distance is more gradual, remaining above −0.1 N up to roughly 20 mm. The five sweeps show close overlap in both full and zoomed views.

The mean ± standard deviation plot again indicates minimal variability, confirming that the alignment procedure and sweep protocol reliably capture the robot–magnet force profile.

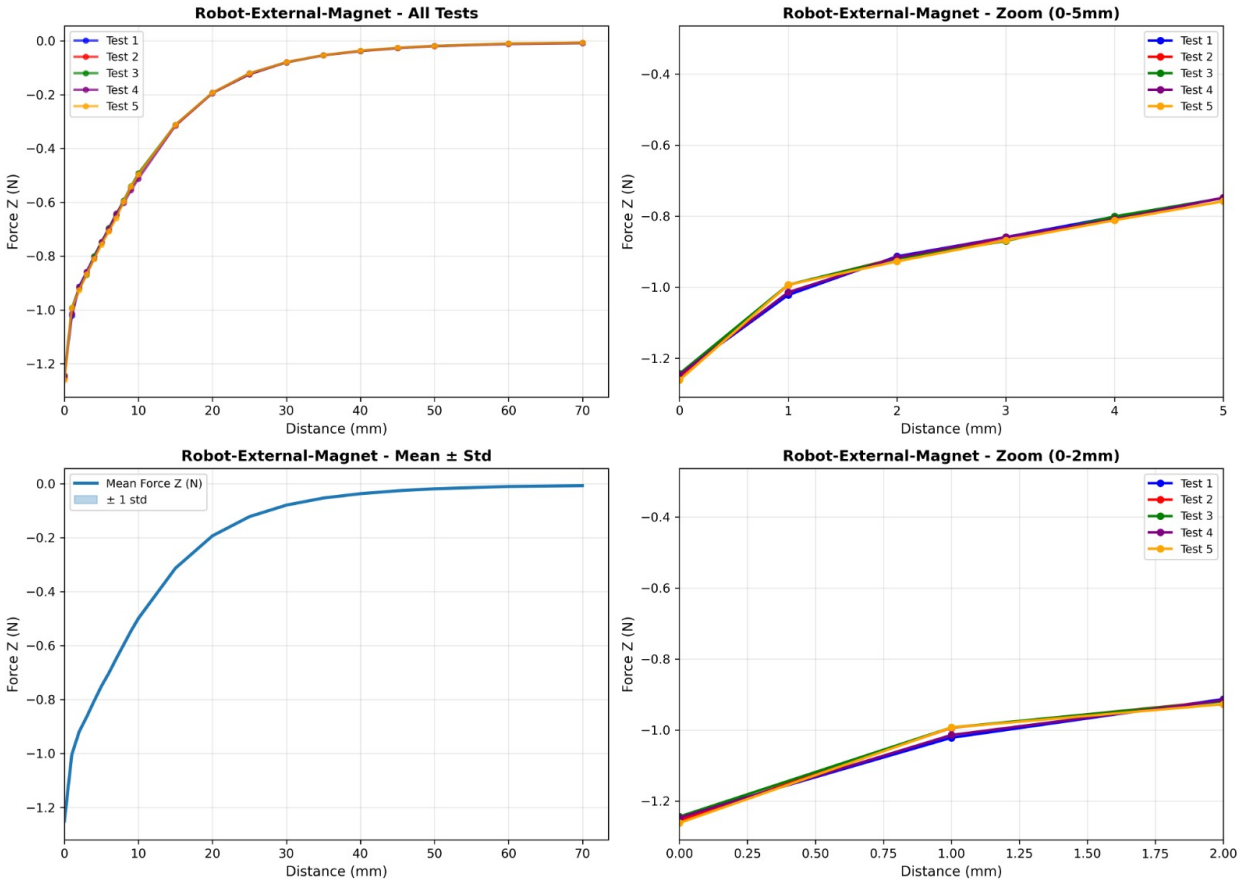

Figure 24: Robot–external-magnet magnetic interaction forces across five repeated trials. Top: all five repeated sweeps (left) and zoomed view of the 0–5 mm region (right). Bottom: mean curve with shaded ±1 standard deviation (left) and zoomed comparison of individual sweeps in the 0–2 mm region (right). Peak force at near-contact: -1.2 ± 0.05 N. The close overlap across all runs demonstrates highly repeatable robot–magnet interaction measurements.

4.1.2 Comparison between COMSOL and experimental data

Figure 25 compares the averaged experimental forces with the COMSOL predictions for both interaction types. For the robot–robot case (left), the simulation accurately reproduces both the peak near-contact force and the rapid decay over the first few millimetres. Minor discrepancies at the smallest gaps ($r < 5$ mm) likely arise from surface roughness and slight angular misalignment, which effectively reduce the physical gap in experiments but are absent in the idealized model. Beyond 5 mm, the COMSOL predictions closely match the experimental measurements across the full range.

For the robot–external-magnet case (right), COMSOL captures the overall trend but systematically underestimates the attraction force at small gaps ($r < 10$ mm). At near-contact, the experimental force reaches approximately −1.2 N, while the simulation predicts approximately −0.75 N, representing a 40% underestimation. Beyond $r = 15$ mm, experimental and simulated curves converge and become nearly indistinguishable. The persistent underestimation at small gaps is consistent with the idealized cylindrical

magnet model in COMSOL not fully capturing edge effects, surface magnetisation variations, and remanence tolerances present in the real N45 cylindrical magnet.

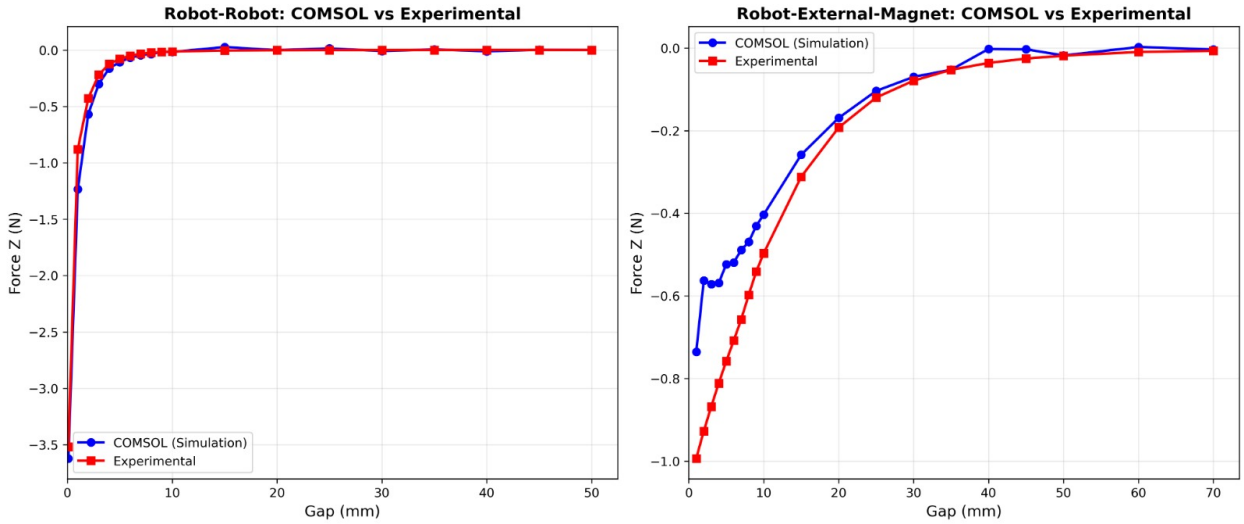

Figure 25: Comparison between COMSOL simulations and experimental force–distance curves. Left: robot–robot interaction showing close agreement across the full measured range, with minor deviations only at $r < 5$ mm. Right: robot–external-magnet interaction showing good overall agreement but systematic underestimation of 40% at small gaps ($r < 10$ mm). COMSOL captures dominant trends for both configurations.

The physical basis for these force profiles is illustrated in Figure 26, which shows the simulated magnetic flux density distributions. In the robot–robot configuration (top), the field is highly concentrated between the two rectangular magnet faces, producing strong localised gradients that explain the steep force decay at small separations. In the robot–external-magnet configuration (bottom), the flux distribution is broader and more diffuse, resulting in a more gradual force decay with distance. These field patterns are consistent with the measured force–distance relationships and validate the magnetic field model used in COMSOL.

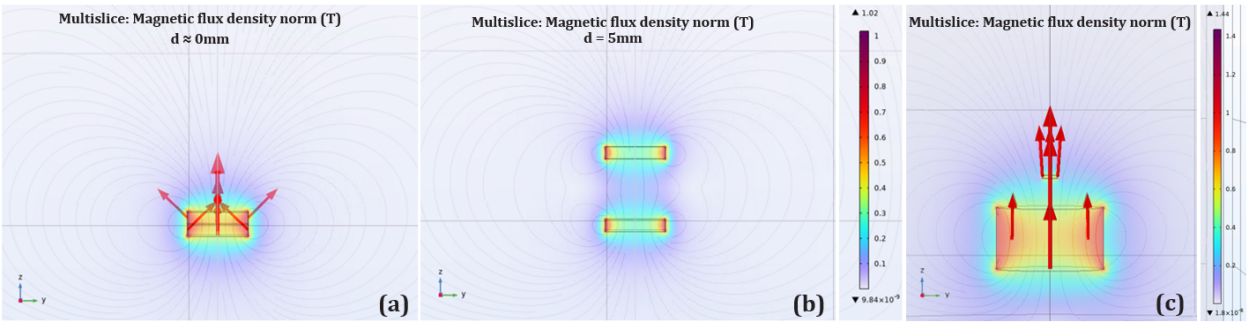

Figure 26: Simulated magnetic flux density distributions ($|\mathbf{B}|$) from COMSOL. **(a)** Robot–robot interaction at near-contact ($d \approx 0$ mm), showing highly concentrated flux between rectangular faces. **(b)** Robot–robot interaction at $d = 5$ mm; the field intensity drops significantly, matching the force decay. **(c)** Robot–external-magnet interaction showing a broader field distribution. Color maps represent the magnetic flux density magnitude in Tesla (T); note that the color scales differ between the robot–robot and robot–magnet configurations.

4.1.3 Validation of force hierarchy requirements

The force measurements establish the magnetic loads that the adhesive interface must resist to satisfy the force hierarchy in Eq. (1). The peak robot–robot coupling force of approximately 3.5 N at near-contact and the robot–external-magnet force of approximately 1.2 N define the minimum required cold-state adhesion: $F_{\text{adh,cold}} > 3.5$ N.

The COMSOL force predictions were validated against these experimental measurements. Robot–robot force predictions closely matched experimental data across the full 0–50 mm range, with only minor deviations at the smallest gaps attributed to surface roughness effects. Robot–external-magnet predictions captured the overall force decay trend but underestimated near-contact forces by approximately 40%, likely due to simplifications in the idealized cylindrical magnet model. Despite this discrepancy, the model successfully predicts the dominant scaling and provides reliable estimates for design purposes.

The validation of whether the measured adhesion forces satisfy the requirement $F_{\text{adh,cold}} > 3.5$ N is presented in Section 4.3.

4.2 Thermal results

Thermal activation performance was evaluated following the screening protocol described in Section 3.6.3. The time required to reach the EVA softening temperature (t_{80} for 80°C) was measured under systematic variation of three parameters: EVA thickness ($h_{\text{EVA}} = \{0.5, 1.0, 2.0\}$ mm), aluminium foil thickness ($h_{\text{Al}} = \{16, 48, 100\}$ µm), and coil distance ($d = \{1, 2, 3, 5\}$ cm). The full screening matrix (36 combinations) is included in Appendix E. The following subsections summarize the measurable trends and identify the optimal configuration.

4.2.1 Heating trends under parameter variation

Effect of EVA thickness. EVA thickness had the strongest influence on heating time. For a fixed foil thickness of 48 µm and coil distance of 1 cm, the time to reach 80°C increased substantially with layer thickness: $t_{80} = 12$ s (0.5 mm), $t_{80} = 40$ s (1.0 mm), and $t_{80} = 52$ s (2.0 mm). Although the 0.5 mm layer produced the fastest responses, it suffered from uncontrolled material overflow when heated above 80°C, resulting in non-repeatable adhesion (detailed in Section 4.2.2). The 2.0 mm layer heated too slowly for practical operation and exhibited robot sinking into the softened adhesive. The 1.0 mm layer provided the best balance between heating speed and geometric stability.

Effect of foil thickness. At a fixed EVA thickness of 1.0 mm and coil distance of 1 cm, increasing aluminium foil thickness consistently reduced t_{80} due to stronger RF coupling. Measured heating times were:

- $h_{\text{Al}} = 16$ µm: $t_{80} = 64$ s
- $h_{\text{Al}} = 48$ µm: $t_{80} = 40$ s
- $h_{\text{Al}} = 100$ µm: $t_{80} = 13$ s

However, the 16 µm foil exhibited weak coupling and often failed to reach 80°C within 120 s. The 100 µm foil produced rapid heating but with undesirable thermal overshoot exceeding 110°C, causing EVA degradation and substrate damage (Section 4.2.2). The 48 µm foil provided reliable heating without overshoot.

Effect of coil distance. For a fixed EVA thickness of 1.0 mm, heating effectiveness was strongly governed by coil distance. Reliable activation into the softening range (80–85°C) was observed only for $d \leq 2$ cm. At $d = 3$ cm and $d = 5$ cm, temperatures stabilized below 70°C within 120 s due to insufficient RF field strength. At $d = 1$ cm with 48 µm foil, $t_{80} \approx 40$ s, providing fast and controllable heating.

4.2.2 Failure modes and rejected configurations

Several parameter combinations were rejected due to thermal or geometric instability observed during screening.

0.5 mm EVA: Material overflow. The thinnest EVA layer (0.5 mm) exhibited uncontrolled material flow when heated above 80°C. Molten EVA spread laterally beyond the 1 cm^2 heating patch, creating irregular adhesive boundaries. In multiple trials, the robot footprint partially lifted from the substrate during cooling, resulting in weak and inconsistent cold-state adhesion. This configuration was rejected despite achieving fast heating times ($t_{80} = 12$ s with 48 µm foil at $d = 1$ cm).

100 µm foil: Thermal overshoot and substrate damage. The thickest aluminium foil (100 µm) produced rapid heating with peak temperatures reaching 110–115°C within 13–20 s at $d = 1$ cm. In two trials with 1.0 mm EVA, small holes (2–3 mm diameter) appeared in the EVA layer.

2.0 mm EVA: Robot sinking and mechanical interlocking. The thickest EVA layer (2.0 mm) required prolonged heating ($t_{80} = 52$ s with 48 µm foil at $d = 1$ cm). During heating, the robot sank partially into the softened adhesive under its own weight and magnetic loading. Upon cooling, the EVA resolidified around the embedded robot body, creating mechanical interlocking that prevented clean detachment even after reheating.

The selected configuration (4.2.3) avoided all three failure modes.

4.2.3 Selected configuration

Based on heating speed, thermal controllability, and geometric stability, the configuration

$$h_{\mathrm{EVA}} = 1.0 \text{ mm}, \quad h_{\mathrm{Al}} = 48 \text{ µm}, \quad d = 1 \text{ cm}$$

was selected for all subsequent locking, unlocking, and assembly demonstrations.

A representative temperature–time curve for this configuration is shown in Fig. 27. The surface reached 80°C in approximately 40 s and 85°C in approximately 55 s, providing reliable entry into the EVA softening range with no temperature overshoot. Five repeated trials demonstrated consistent behaviour with minimal residue accumulation.

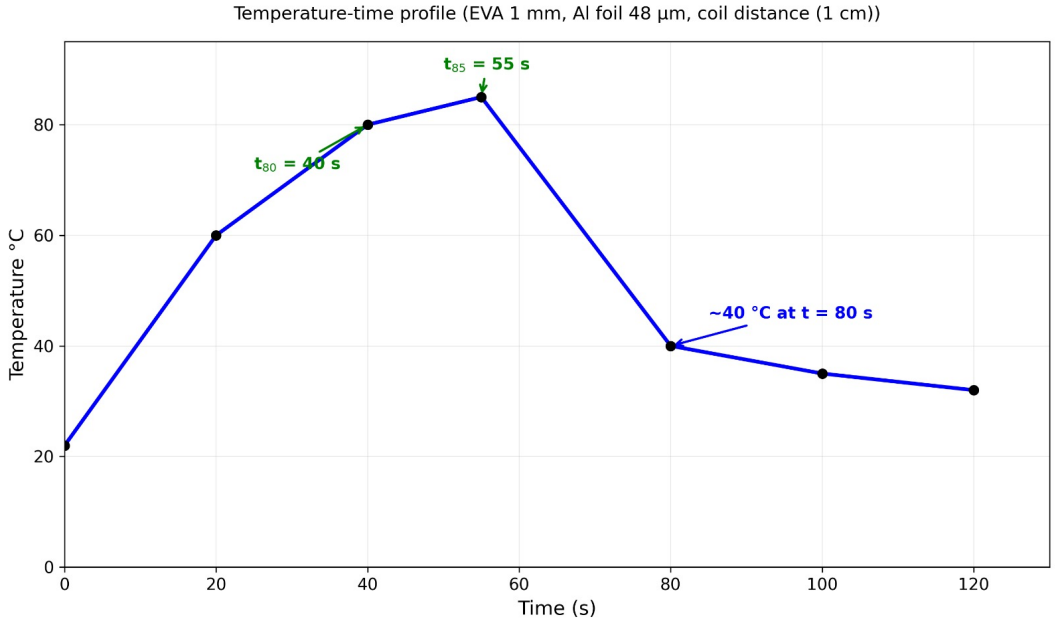

Figure 27: Temperature–time curve for the selected configuration ($h_{\mathrm{EVA}} = 1.0$ mm, $h_{\mathrm{Al}} = 48$ µm, $d = 1$ cm). The surface reaches 80°C in ∼40 s and 85°C in ∼55 s, providing controlled entry into the EVA softening range without overshoot. Passive cooling returns the surface to ∼40°C within 80 s.

4.2.4 Cooling behaviour

Cooling from 80°C to approximately 40°C required roughly 80 s under passive convection. This temperature range was sufficient for the EVA to regain stiffness and re-establish strong cold-state adhesion. During demonstration experiments (Section 4.5), multiple reheating and cooling cycles were performed without observable degradation of the EVA or foil layers.

4.2.5 Summary of screening outcomes

Table 3 summarizes the screening outcomes. The selected configuration (1.0 mm EVA, 48 µm Al, 1 cm distance) provides:

1. Fast heating: $t_{80} \approx 40$ s
2. No thermal overshoot or substrate damage
3. Repeatable geometric stability across multiple cycles
4. Sufficient cooling time (∼80 s) for practical sequential operations

Table 3: Summary of thermal parameter screening results.

Case	Result	Comment
EVA = 0.5 mm	Material overflow	Non-repeatable adhesion
EVA = 2.0 mm	Robot sinks into softened EVA	Mechanical interlocking
EVA = 1.0 mm	**Balanced: consistent, repeatable**	**Final choice**
Foil = 16 µm	Weak RF coupling	$T < 70$ °C
Foil = 48 µm	**Controlled heating to 80 °C in 40 s**	**Final choice**
Foil = 100 µm	Thermal overshoot 110–115 °C	EVA degradation, holes
Coil ≥ 3 cm	Weak field coupling	$T < 70$ °C
Coil = 1 cm	**Fast, controlled heating**	**Final choice**

4.3 Adhesion test results

Adhesion strength was quantified using the test setup described in Section 3.6.4. All measurements were performed on specimens prepared with the selected interface configuration ($h_{\text{EVA}} = 1.0$ mm, $h_{\text{Al}} = 48$ µm) following identical thermal bonding procedures: RF heating to 80–85°C, magnetic pressing, and passive cooling to 40°C.

Two loading modes were evaluated: (i) normal pull-off (Z-direction) and (ii) in-plane shear loading (X direction). Three independent specimens were tested for each mode ($n = 3$).

4.3.1 Cold-state adhesion force

Figure 28 shows the measured force–displacement curves for both loading modes. In the normal pull-off tests (Fig. 28a), peak detachment forces were 5.26 N, 5.52 N, and 5.43 N, producing a mean of 5.40 N and standard deviation of 0.13 N (2.4%). The curves exhibit the expected behaviour: a gradual linear rise governed by elastic deformation of the TPU robot and EVA layer, followed by an abrupt force drop upon interfacial failure.

Specimen 1 exhibited substantially greater extension before failure (7.5 mm) compared to Specimens 2 and 3 (4.5 mm), likely due to minor variations in EVA thickness or robot bonding depth during specimen preparation. Despite this geometric difference, the peak detachment forces remained highly consistent across all three specimens (standard deviation 2.4%), confirming repeatability of the interfacial adhesion strength.

In the shear tests (Fig. 28b), peak forces were 7.22 N, 7.76 N, and 6.64 N, corresponding to a mean of 7.21 N and standard deviation of 0.46 N (6.4%). These curves contained characteristic stick–slip oscillations prior to detachment, indicative of micro-slip events at the EVA interface under in-plane loading.

In both loading modes, the cold-state adhesion force substantially exceeded the peak robot–robot magnetic coupling force of approximately 3.5 N measured in Section 4.1, confirming that the force hierarchy requirement $F_{\text{adh,cold}} > F_{AB}$ from Eq. (1) was satisfied.

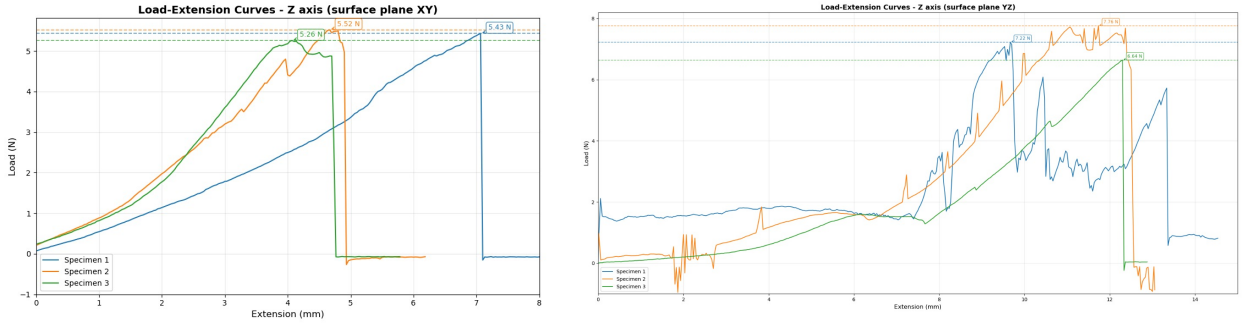

(a) Normal (Z-direction)

(b) Shear (X-direction)

Figure 28: Cold-state adhesion force–displacement curves for three specimens tested in (a) normal pull-off (Z-direction) and (b) in-plane shear (X-direction).

Table 4: Summary of cold-state adhesion forces for the selected EVA–foil interface configuration.

Direction	n	**Mean force [N]**	**Range [N]**
Normal (Z)	3	5.40 ± 0.13	5.26–5.52
Shear (X)	3	7.21 ± 0.46	6.64–7.76

4.3.2 Hot-state adhesion

Hot-state adhesion was not directly measured, as the EVA layer cools below 40°C within approximately 80 s after heating (Section 4.2). Above 80–85°C, the EVA layer melts and becomes too soft to maintain adhesion. Therefore, the effective interface strength is negligible, and we take $F_{\text{adh,hot}} \approx 0$ for the analysis.

4.3.3 Repeatability

Each specimen was tested once to avoid history-dependent effects such as partial residue transfer. Across all samples, no visible EVA damage and negligible residue were observed after detachment. These results, combined with the multi-cycle thermal actuation tests reported in Section 4.2.3, indicate that the EVA–foil interface tolerates repeated locking and unlocking cycles without measurable degradation.

4.4 COMSOL deformation

Magneto-mechanical deformation of a single robot and a six-robot ring was analysed using the COMSOL setup described in Section 3.7.2. As introduced in Section 3.4.2, the robot body contains three embedded N45SH magnets in the asymmetric $(+,-,-)$ configuration and compliant flexure points at the vertices that enable controlled shape change under magnetic loading.

This deformation behaviour (referred to as "pinching" (Fig. 12c)) occurs when the semicircular grooves at the vertices act as compliant hinges, allowing the hexagon to narrow as the corners fold inward under magnetic loading. The hexagonal faces remain relatively straight, with the embedded magnets providing local stiffening to faces 0, 2, and 4.

Uniform magnetic fields were applied in the $+y$ direction (vertical, upward), and stationary parametric sweeps over field magnitude B_0 were performed. Magnetic forces computed via the `Force Calculation` nodes were coupled to the *Solid Mechanics* interface to predict deformation. Two loading scenarios were examined: (i) net-dipole loading (all three magnets active simultaneously) to represent the full robot response, and (ii) six-robot ring deformation to evaluate collective behaviour relevant for gripping applications. Single-magnet activation results are provided in Appendix F.

4.4.1 Single-robot deformation under uniform fields

All three magnets were activated simultaneously, representing the net dipole moment of the robot ($\mathbf{m}_{\text{net}} = 2m_0\hat{\mathbf{x}}$ from Eq. 4).

Figure 29a shows the progression of deformation from 30 to 500 mT. At 30 mT and 50 mT, deformation remains minimal. Visible deformation becomes apparent above 50 mT and increases monotonically with field strength. At 500 mT, the robot exhibits approximately 19% height reduction, with pronounced hinge bending at the flexure points and downward collapse of the top face.

Figure 29b quantifies the vertical displacement of a reference point on the robot top edge. The displacement reaches approximately 5.5 mm at 500 mT.

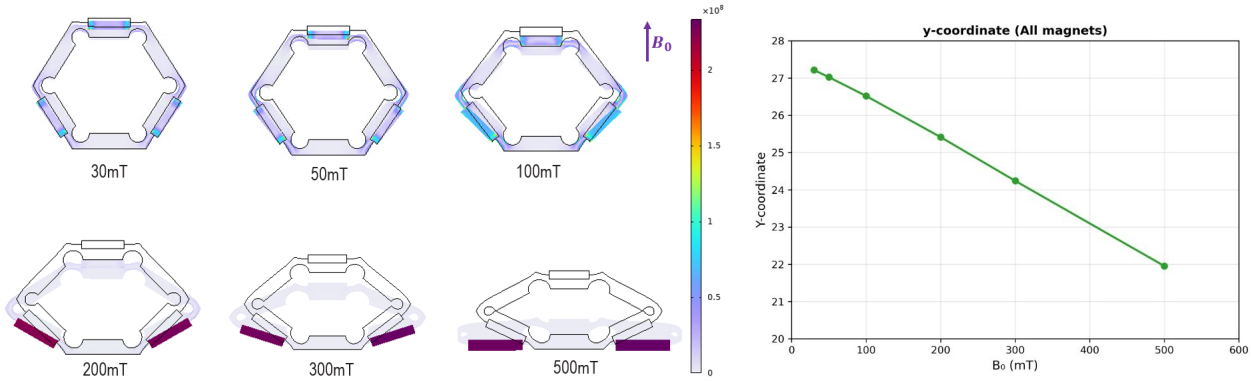

(a) Deformation with all three magnets active

(b) Vertical displacement vs. B_0

Figure 29: Single-robot deformation with all three magnets active. **(a)** Deformation progression from 30 to 500 mT. Colors represent **von Mises stress** (0 to 2.5×10^8 N/m^2) on a **white-to-purple scale**. White regions are relaxed, while dark purple regions indicate high stress concentrations at the magnet interfaces and the compliant hinges. **(b)** Vertical displacement of a top-edge reference point, reaching approximately 5.5 mm at 500 mT (19% height reduction).

4.4.2 Ring deformation

A six-robot ring was simulated with one robot polarity-reversed (top robot: $(-,+,+)$ configuration; all others: $(+,-,-)$) to generate a net dipole moment for the assembly, following the actuation logic described in Section 3.5.2. The bottom boundary was constrained to mimic the anchored EVA surface. All three magnets of the polarity-reversed robot were activated.

The magnetic flux density plot (Fig. 30a) reveals strong magnetic coupling between the robots. High field intensity (cyan regions) bridges the air gaps between adjacent magnets, confirming that the magnetic attraction forces are effectively maintaining the ring integrity under bending and gravity.

The First Principal Strain distribution (Fig. 30b) shows strain concentrating at the vertices (cyan/light blue regions) and inter-robot contacts. The magnets themselves (dark blue regions) exhibit minimal strain, confirming they act as rigid links while deformation occurs at the designed flexure points.

At 100 mT, the ring shows modest upward bending with slight lateral displacement due to asymmetric torque from the reversed-polarity robot. Simulations above 100 mT encountered convergence issues due to multi-body contact complexity. The result validates that polarity reversal generates collective actuation torque and that the compliant hinge design distributes deformation across multiple flexure points.

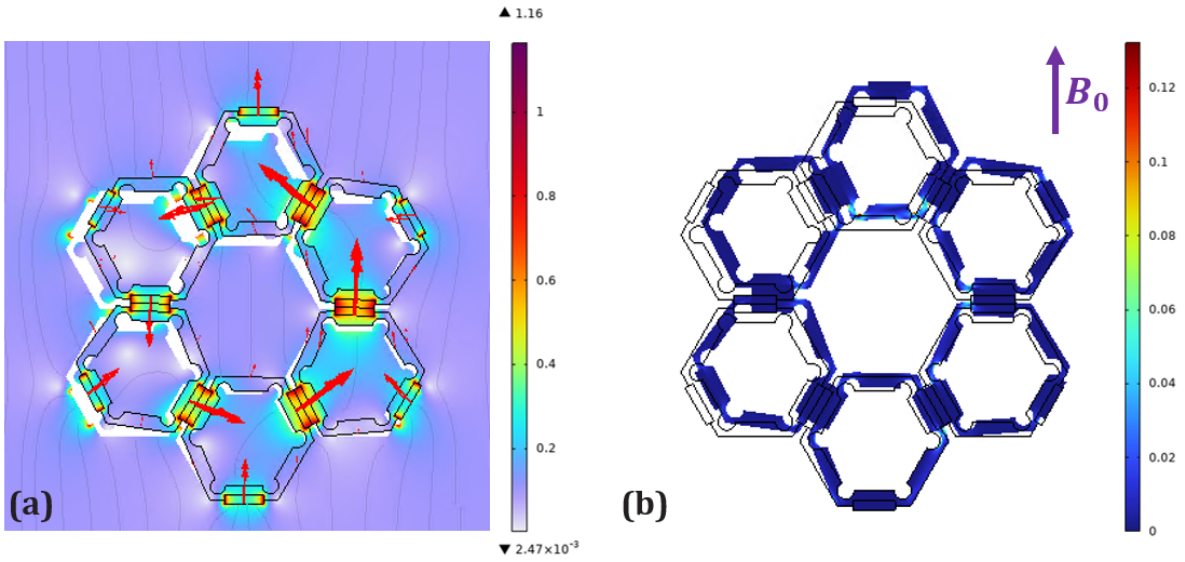

Figure 30: Six-robot ring deformation at $B_0 = 100$ mT with one polarity-reversed robot (top position). **(a)** Magnetic flux density showing strong coupling between adjacent robots. **(b)** First principal strain. High strain (cyan/light blue) concentrates at vertices and contacts; magnets (dark blue) remain rigid.

4.5 Demonstration results

This section reports proof-of-concept demonstrations of the system capabilities introduced in Section 3.8. The experiments validate (i) the range of static assemblies achievable through magnetic self-organization, (ii) selective thermal anchoring and release on the EVA–foil substrate, and (iii) collective rotation of single robots and ring assemblies under uniform magnetic fields.

4.5.1 Static assembly configurations

Figure 31 shows the assembly configurations achieved through magnetic coupling. Panel (a) shows single-robot vertical compression under an external cylindrical magnet, with height reducing from approximately 15 mm to 7 mm (53% reduction). This reduction is substantially larger than the COMSOL prediction of 19% (Section 4.4) because the hand-held magnet exerts strong gradient forces that actively compress the robot, whereas the simulation applied only a uniform aligning torque.

Panels (b–d) show small ring assemblies formed by magnetic self-organization with 4, 5, and 6 robots, respectively. These maintain regular hexagonal packing. Panel (e) demonstrates a larger 10-robot ring; as the ring size increases, the structure exhibits higher compliance and slight geometric variations due to accumulated tolerances. Panel (f) shows a line assembly in a head-to-tail configuration.

4.5.2 Selective thermal anchoring and release

Selective anchoring was demonstrated through progressively more complex assemblies: two-robot locking, multi-robot lines, and closed rings.

Two-robot primitive. Figure 32 shows the elementary locking–unlocking sequence over nine experimental frames. Robot A was magnetically guided to a heated EVA spot (frames 1–2), pressed into the softened adhesive (frame 3), and became firmly anchored after passive cooling to 40°C (frame 4). Robot B was then magnetically steered to Robot A and locked magnetically (frame 5). Subsequently, Robot B was unlocked solely through magnetic actuation (frames 6–7), confirming that the magnetic link can be broken without affecting the thermal anchor. Finally, a heating pulse beneath Robot A released it from the substrate (frames 8–9).

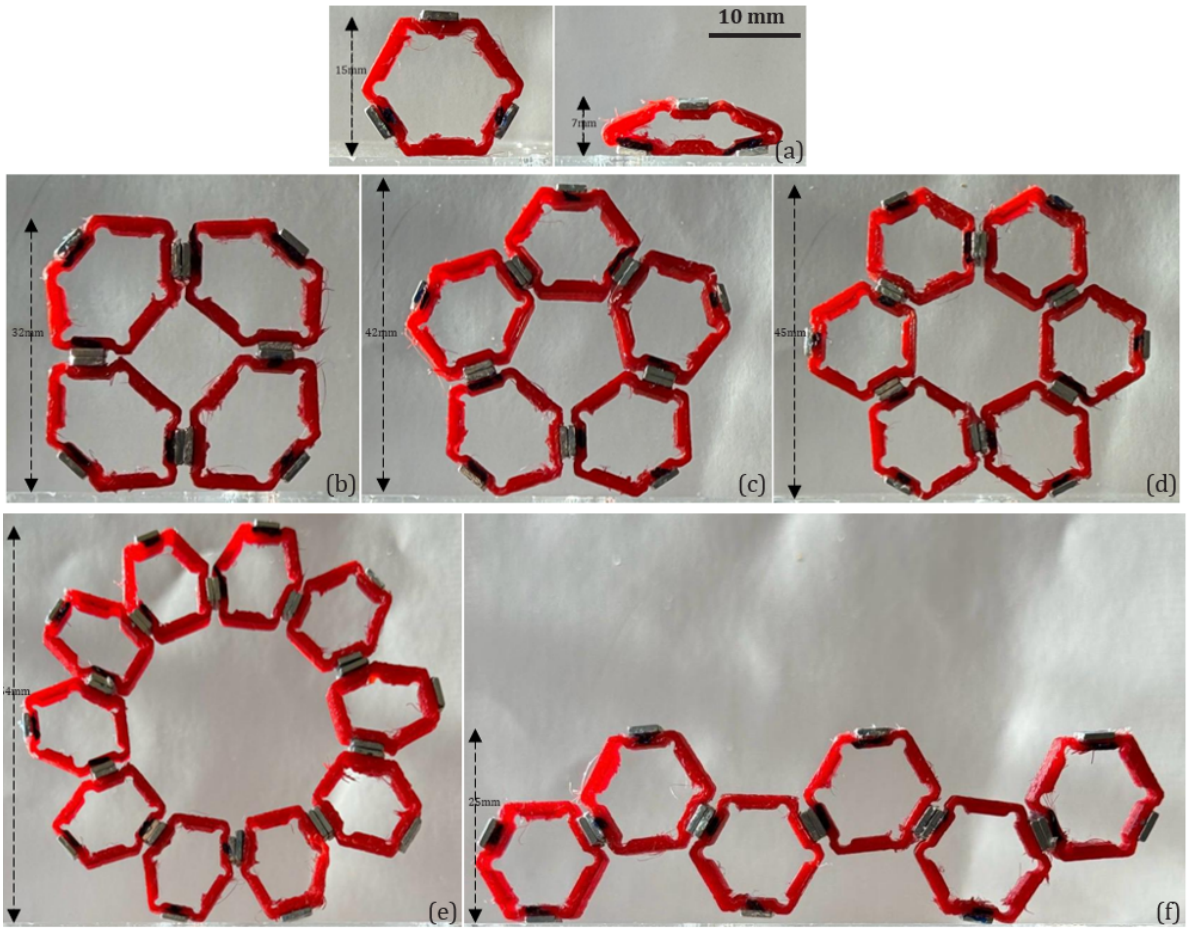

Figure 31: Assembly configurations and deformation capabilities. (a) Single-robot vertical compression under external cylindrical magnet. (b–d) Stable ring assemblies with 4, 5, and 6 robots. (e) Large-scale ring assembly with 10 robots. (f) Line assembly in head-to-tail configuration.

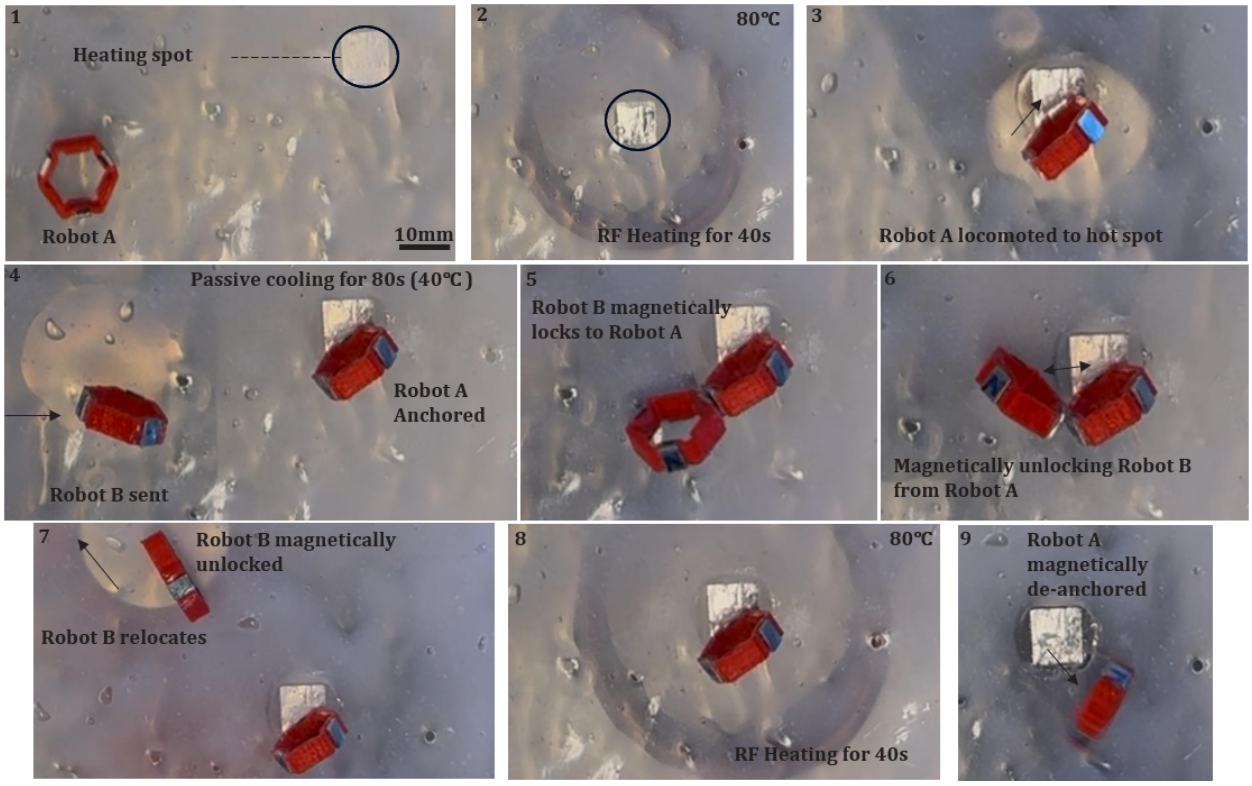

Figure 32: Two-robot locking and unlocking sequence on the EVA–foil substrate. Frames 1–4: Robot A is thermally anchored to the heated substrate. Frames 5–7: Robot B magnetically locks to Robot A and is subsequently unlocked via magnetic actuation. Frames 8–9: Robot A is released by reheating its anchoring point.

Line formation. Figure 33 demonstrates the assembly of a six-robot chain over 13 experimental frames. Robot A was first anchored (frames 1–4), then Robots B–F were sequentially added in a head-to-tail configuration along the magnetic dipole axis (frames 5–11). Throughout assembly, Robot A remained fixed while additional robots locked magnetically to the previous member. A heating pulse beneath Robot A released the entire chain (frames 12–13), enabling coordinated locomotion of the assembled structure.

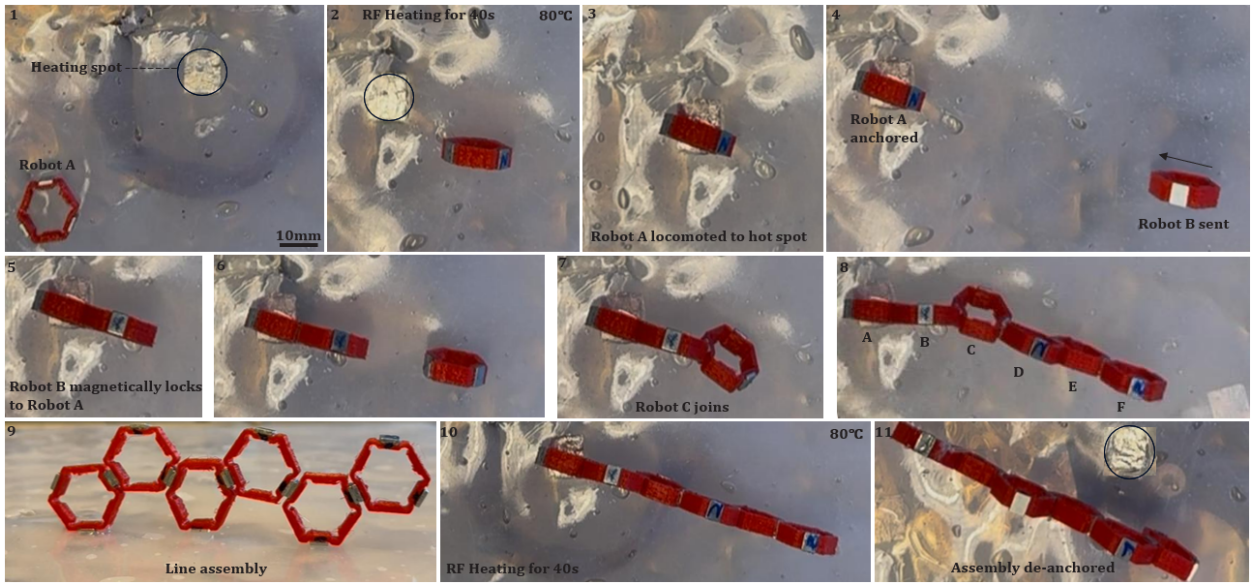

Figure 33: Six-robot line formation and collective release. Robot A is anchored (frames 1–4), then Robots B–F are added sequentially to form a chain (frames 5–11). Local reheating beneath Robot A releases the entire assembly (frames 12–13).

Ring assembly. Figure 34 shows the formation of a five-robot ring over 13 experimental frames. First, Robot A was thermally anchored (frames 1–4). Subsequently, Robots B–E were sequentially added, magnetically locking to Robot A and to each other to form a rigid closed loop (frames 5–10). Once the ring was complete, the entire assembly remained secured by the single anchor point at Robot A. Finally, a heating pulse beneath Robot A released the anchor (frame 13), freeing the fully formed ring to locomote as a collective unit.

4.5.3 Rotation under uniform magnetic fields

Rotation behaviour under uniform magnetic fields was evaluated using the PacMag Helmholtz coil system. Figure 35 shows rotation sequences for a single robot and multi-robot ring assemblies under slowly rotating uniform fields ($B_0 = 12$–15 mT).

Panel (a) shows a single robot rotating coherently with the external field ($B = 2$ mT), validating the basic magnetic alignment mechanism. Panels (b–d) show ring assemblies of 5–7 robots, each with one robot polarity-reversed to create a net dipole moment. These asymmetric rings exhibited coherent rotation about their geometric centre.

Five- and six-robot rings (panels b, c) achieved repeatable rotation. Seven-robot rings (panel d) also rotated but exhibited increased wobble and occasional shape distortion compared to smaller rings. The timestamps indicate a rotation speed consistent with the applied field frequency.

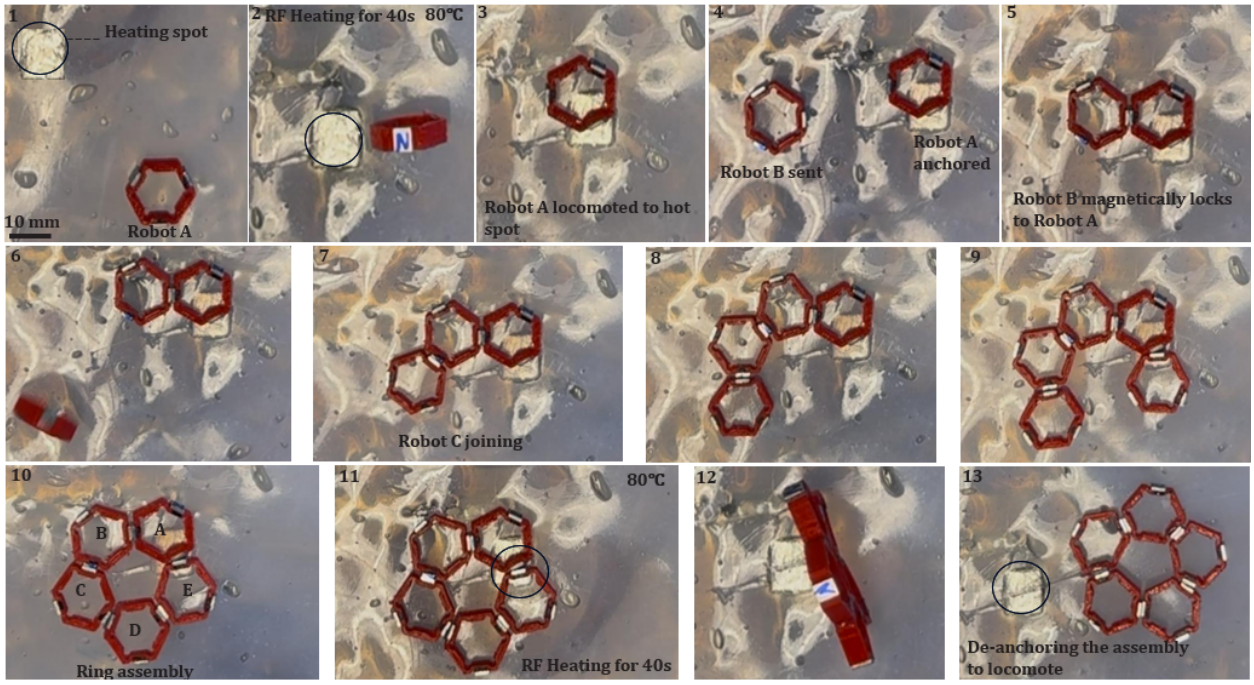

Figure 34: Five-robot ring formation and collective release. Robot A is thermally anchored (frames 1–4), serving as the fixed base. Robots B–E are added sequentially to form a closed, magnetically interlocked ring (frames 5–10). Finally, reheating the substrate beneath Robot A de-anchors the entire assembly, allowing the ring to move as a single unit (frames 11–13).

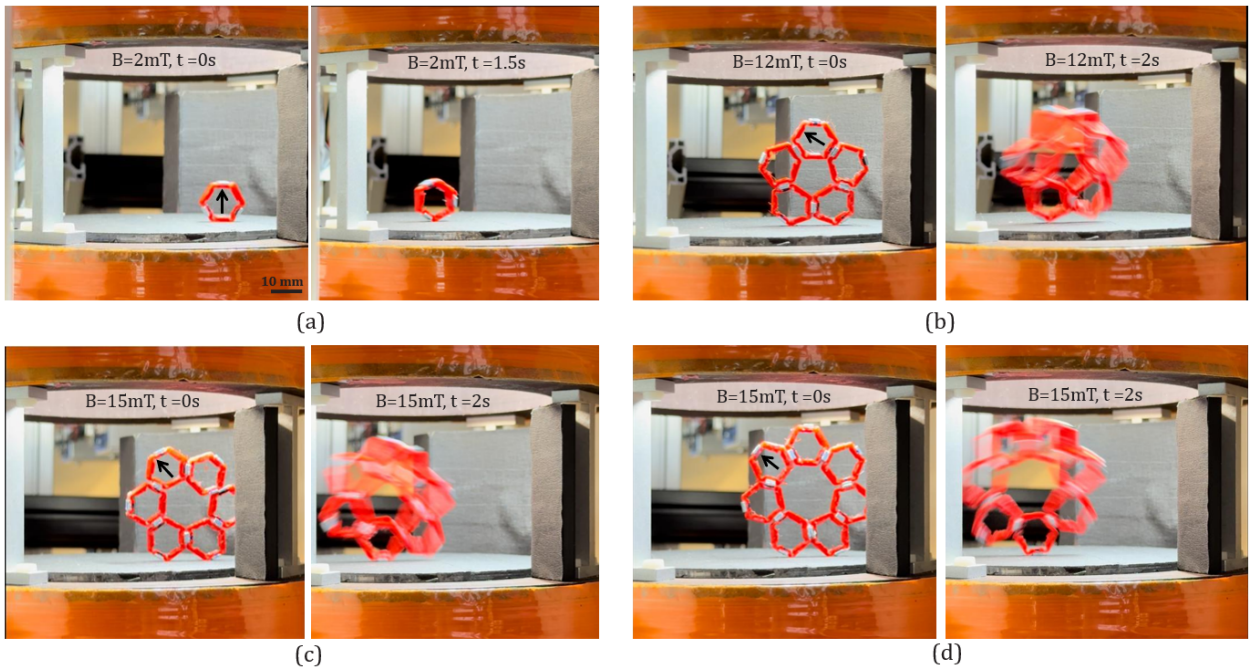

Figure 35: Rotation of single and multi-robot assemblies under slowly rotating uniform magnetic fields in the Helmholtz coil. (a) Single robot rotates coherently ($B = 2$ mT). (b) Five-robot ring with one polarity-reversed robot achieves stable rotation ($B = 12$ mT). (c) Six-robot ring rotates under the same conditions ($B = 15$ mT). (d) Seven-robot ring exhibits rotation ($B = 15$ mT) but with reduced stability and transient shape distortions.

5 Discussion

This work demonstrated a modular magnetic soft robotic system capable of selective locking, unlocking, and cooperative motion through the integration of magnetic actuation and thermally reversible adhesion. The results collectively validate the core hypothesis: that dual-stimulus control (combining magnetic fields for locomotion and assembly with thermal activation for selective anchoring) enables on-demand reconfiguration of multi-robot assemblies. This discussion examines the physical mechanisms underlying the observed behaviours, evaluates performance trade-offs and limitations, and considers implications for potential applications.

Magnetic force measurements and COMSOL validation. The experimental force characterisation established the magnetic interaction profiles necessary for design validation and provided a benchmark for finite-element predictions. For robot–robot interactions, COMSOL predictions closely matched experimental measurements across the full 0–50 mm range, with only minor deviations at gaps below 5 mm. These small discrepancies likely arise from surface roughness and slight angular misalignment in the physical setup, which effectively reduce the real gap compared to the idealized model. This close agreement validates the magnetic model and provides confidence that the simulated magnetic coupling forces ($F_{AB} \approx 3.5$ N at near-contact) accurately represent the operational loads that the adhesive interface must resist.

For robot–external-magnet interactions, COMSOL captured the overall force decay trend but systematically underestimated attraction forces by approximately 40% at small gaps (experimental: 1.2 N; simulated: 0.75 N at near-contact). This underestimation is consistent with the idealized cylindrical magnet model not fully capturing edge effects, surface magnetisation variations, and remanence tolerances present in the physical N45 magnet. Despite this quantitative discrepancy, the high repeatability of experimental measurements (five trials) confirms that the actual robot–magnet forces are predictable and reliable. Since the qualitative scaling trend is correctly captured, the model remains useful for design purposes and correctly predicts the dominant physics governing magnetic actuation. This discrepancy did not affect design decisions, as experimental validation provided the necessary force values for establishing the adhesion requirements.

Thermal parameter selection and failure mechanisms. The thermal screening results revealed a narrow window of acceptable parameter combinations, with only the 1.0 mm EVA, 48 µm aluminium foil, and 1 cm coil distance configuration providing balanced performance. The failure modes observed for rejected configurations illuminate the underlying physical constraints. The 0.5 mm EVA layer exhibited uncontrolled material overflow when heated above 80°C because the thin polymer film lacks sufficient thermal mass to distribute heat evenly, leading to localised overheating. This resulted in irregular adhesive boundaries and weak, inconsistent cold-state bonding as the robot footprint partially lifted during cooling.

Conversely, the 2.0 mm EVA layer required prolonged heating (52 s to reach 80°C) due to the greater thermal mass. During this extended heating period, the robot sank into the softened adhesive under its own weight and magnetic loading, creating mechanical interlocking as the EVA resolidified around the embedded robot body. This demonstrates that EVA thickness must be balanced: thick enough to provide stable adhesion without overflow, yet thin enough to heat and cool rapidly without allowing robot embedment. The selected 1.0 mm thickness represents this compromise, achieving $t_{80} \approx 40$ s heating and ∼80 s passive cooling with timescales practical for sequential multi-robot operations.

The 100 µm aluminium foil produced rapid heating (13 s) but with a dangerous thermal overshoot exceeding 110°C, causing localised EVA degradation and substrate damage (2–3 mm diameter holes observed in two trials). This confirms that foil thickness directly controls RF coupling strength and must be carefully selected to avoid exceeding the EVA thermal degradation threshold while still achieving adequate heating speed. The 48 µm foil provided the optimal balance, reaching 80–85°C without overshoot.

These findings suggest a general design principle: the adhesive layer thickness must be sufficient to provide adequate thermal mass to buffer rapid RF heating, while remaining thin enough to limit viscous sinking during the activation window. For the current robot scale (characteristic dimension ∼1.5 cm), a 1.0 mm interface proved optimal.

Force hierarchy and selective anchoring. The measured cold-state adhesion forces (5.40 N normal, 7.21 N shear) substantially exceed the peak robot–robot magnetic coupling force (3.5 N), establishing a ratio

of approximately 1.5:1 for normal loading and 2.1:1 for shear. This margin proved sufficient throughout all demonstration experiments: anchored robots remained fixed during magnetic manipulation of neighbouring robots, and no unintended detachments occurred. The higher shear adhesion compared to normal pull-off is characteristic of viscoelastic adhesives like EVA, where in-plane loading mobilizes a larger effective contact area and allows stress redistribution through micro-slip events (evidenced by the stick–slip oscillations in the shear test curves). This directional dependence is beneficial for the system, as magnetic manipulation typically involves in-plane forces, providing an additional safety margin against accidental detachment during assembly.

The extension variation observed in Specimen 1 (7.5 mm vs 4.5 mm for Specimens 2–3, despite consistent peak forces) indicates minor geometric variability in EVA thickness or robot bonding depth during manual specimen preparation. While this represents a manufacturing tolerance issue that could be addressed through improved process control, the consistency of peak detachment forces (standard deviation 2.4%) confirms that interfacial adhesion strength itself is repeatable and reliable.

Hot-state adhesion was not directly measured due to practical constraints: the RF heating setup and tensile testing equipment were located in different laboratories, and EVA cools from 80°C to below 40°C within approximately 80 s, making transport between facilities impractical. However, the successful selective detachments demonstrated throughout Section 4.5 provide indirect evidence that $F_{\text{adh,hot}}$ is sufficiently low to allow magnetic forces to overcome the softened interface. For the force balance requirement $F_{\text{adh,hot}} < F_{\text{magnetic}}$ to enable detachment, the exact value is less critical than confirming it falls well below the magnetic actuation forces, which was validated experimentally through repeatable locking–unlocking cycles.

Deformation simulations and field strength threshold. The COMSOL deformation predictions revealed a critical field strength threshold: no visible deformation occurred below 50 mT in any simulation configuration (single-magnet, or ring assembly). This finding directly explains the experimental observation that the Helmholtz coil system (maximum 50 mT uniform field) could achieve controlled rotation without inducing pinching behaviour. While this limitation prevented experimental validation of deformation under uniform fields, it confirms that the compliant hinge design requires field strengths above 100 mT to produce substantial shape change (>10% height reduction).

This threshold has important implications for system design and applications. For tasks requiring rigid-body rotation without deformation, such as positioning or reorientation during assembly, the 10–50 mT range is ideal, as demonstrated by the stable rotation of 5–6 robot rings. For applications requiring active gripping or adaptive navigation through deformation, higher-field actuation systems (>100 mT uniform fields or localised gradient fields) would be necessary. Alternatively, achieving pinching at lower fields could be explored through material substitutions (softer TPU Shore 65A instead of 85A, or silicone elastomers with lower elastic modulus) or geometric modifications (thinner wall sections, deeper hinge grooves, or reduced overall robot height to increase compliance).

The substantial discrepancy between simulated (19% at 500 mT) and experimental (53%) height reduction arises from three factors. First, the COMSOL simulations employed uniform vertical fields, whereas the experimental cylindrical magnet creates a highly non-uniform gradient field with localised high-intensity regions potentially exceeding 200 mT near the magnet surface. This gradient field produces position-dependent forces that induce more complex, asymmetric deformation modes than the symmetric pinching predicted under uniform loading. Second, the 2D plane-stress model assumption cannot capture three-dimensional buckling modes and through-thickness stress variations that likely contribute to the experimental collapse. Third, in experiments the robot is compressed against a rigid surface. As the structure collapses, the robot body interacts with this surface through friction and direct contact support, which constrains the deformation. In contrast, the COMSOL model treats the robot as a free-standing body with only the central bottom face fixed, neglecting the contact mechanics and frictional forces that occur when the structure is pressed against a physical boundary.

Despite these quantitative differences, the simulations successfully validate the fundamental design concept: the semicircular grooves at vertices act as compliant hinges that enable controlled, monotonic deformation with increasing field strength. The qualitative agreement (progressive hinge bending, stress concentration at flexure points, and asymmetric response consistent with the three-magnet configuration) confirms that the robot geometry functions as intended. The simulations thus provide valuable predictive insight into the field strength range required for observable deformation, even if absolute deformation magnitudes

remain approximate.

Assembly formation and size-dependent stability. The demonstration experiments confirmed that magnetic self-organization produces stable assemblies (rings and lines) without requiring precise positioning control. Rings of 5–6 robots maintained regular hexagonal packing and exhibited stable rotation under uniform fields when one robot was polarity-reversed to create a net dipole moment. However, larger assemblies (7+ robots) showed increased wobble and occasional shape distortion during rotation. This reduced stability arises from two competing effects: higher total mass increases rotational inertia and gravitational loading on the compliant TPU structure, while the magnetic torque available for rotation remains approximately constant (determined by the single reversed-polarity robot's net dipole). Additionally, the low surface friction of TPU-85A on the setup surface provides minimal resistance to sliding, unlike silicone elastomers which exhibit higher surface adhesion and could potentially stabilize larger assemblies through substrate contact.

The practical assembly size limit observed in this work (stable rotation up to 6–7 robots) may be sufficient for many biomedical applications where compact modular structures are advantageous. However, scaling to larger assemblies would require design modifications such as increased robot magnetisation, stiffer structural materials to resist gravitational sagging, or active stabilization through enhanced substrate adhesion.

Line assemblies exhibited similar magnetic locking behaviour to rings. However, line rotation was not pursued further because the application requirements do not necessitate rotating linear chains. For the intended use cases (sequential assembly, targeted delivery, or modular structures) translation and reconfiguration are more relevant than rotation. Rings proved more practical for demonstrating collective rotation due to their closed-loop topology, which distributes mechanical loads symmetrically and provides inherent structural stability.

Thermal selectivity and spatial resolution. The RF heating system achieved adequate spatial selectivity for the demonstration tasks: the 1 cm^2 heating spot could reliably target individual robots (characteristic dimension 1.5 cm) within assembled structures. Throughout line and ring formation experiments, no accidental heating of neighbouring robots was observed, even in tight hexagonal packing. This confirms that thermal selectivity is preserved even when multiple magnetic contacts are present, enabling partial detachment operations. For instance, a robot anchored in the middle of a line assembly could be selectively released while neighbouring robots remained magnetically locked.

The demonstrated locking–unlocking sequences validate that the force hierarchy $F_{\text{adh,cold}} > F_{AB} > F_{\text{adh,hot}}$ enables reliable selective control: anchored robots resisted magnetic perturbations from assembly operations, yet released cleanly upon reheating. The 40 s heating and 80 s cooling timescales, while slower than purely magnetic reconfiguration, fall within practical limits for sequential multi-robot tasks.

Advantages over prior approaches. The system developed in this work offers several advantages over existing magnetic soft robot designs. Compared to purely magnetic systems that lack selective anchoring mechanisms, the integration of thermally reversible adhesion enables robots to be fixed in place during assembly operations, preventing unintended motion and allowing sequential construction of complex multi-robot structures. This selective locking capability is not achievable with magnetic forces alone, as magnetic interactions are always bilateral and cannot selectively immobilize individual robots within a swarm.

Compared to mechanical locking systems (e.g., shape-memory alloy latches, electro-adhesive pads, or pneumatic grippers), thermal adhesion via EVA provides reversible, low-power locking without requiring robot-integrated actuation hardware. The external RF heating approach eliminates the need for power supplies or electrical connections, reducing robot complexity and enabling simpler, smaller designs. The demonstrated heating times (40 s) and cooling times (80 s) are comparable to many thermally activated shape-memory polymer systems, while the adhesive interface exhibits minimal degradation over multiple cycles.

The three-magnet asymmetric configuration enables both controlled rotation and deformation, providing multifunctional actuation from a single robot design. This design approach, using a geometric arrangement of identical magnetic elements to programme different behaviours, offers a pathway toward scalable fabrication compared to approaches requiring heterogeneous materials or complex embedded electronics in each robot.

Limitations of the current work. This work has several limitations that constrain the generalisability and immediate applicability of the results.

First, the system relies entirely on external magnetic fields for actuation. This design was chosen to achieve untethered operation, which is a critical requirement for minimally invasive medical robots where onboard batteries and electronics are often impractical due to size and biocompatibility constraints. The limitation is not the absence of physical tethers, but that the operational workspace is restricted to regions accessible by the external field generator (e.g., within the Helmholtz coil volume or within reach of handheld permanent magnets). This approach is standard in biomedical applications such as magnetically guided capsule endoscopy, but restricts operation to controlled clinical environments. Additionally, the RF heating system required close working distance (1 cm) for rapid activation ($t_{80} \approx 40$ s). Achieving similar heating at clinically relevant distances (5–10 cm) would require a more powerful RF generator.

Second, the COMSOL deformation model employed simplified 2D plane-stress and linear-elastic assumptions. While sufficient to validate the compliant hinge design and identify the critical field strength threshold, the model cannot capture three-dimensional buckling or the nonlinear behaviour of TPU-85A at large deformations (>50% compression). The simulations identified that substantial deformation (>10% height reduction) requires uniform field strengths exceeding 100 mT. This threshold explains why controlled pinching could not be demonstrated experimentally: the PacMag Helmholtz coil system is limited to 50 mT maximum field, which falls below the threshold required for observable shape change.

Third, all experiments were conducted on flat acrylic surfaces with EVA–foil substrates. The EVA layer served as a functional analogue to demonstrate that thermally reversible adhesion can provide selective anchoring under magnetic fields. However, this simplified substrate does not replicate clinical conditions: biological tissues are curved, compliant, wet surfaces covered with mucus and subject to dynamic motion. Translation to medical applications would require biocompatible alternatives such as mucoadhesive coatings that maintain adhesion in fluid environments and exhibit thermal reversibility, which are topics addressed in 6. Furthermore, the current prototypes use commercial-grade TPU-85A and N45 magnets that have not undergone biocompatibility testing. Medical deployment would require material redesign and validation, which were beyond the scope of this proof-of-concept work.

Fourth, several quantitative investigations were omitted due to time constraints. Full parametric characterization of assembly performance, three-dimensional contact simulations, and gradient field modeling in COMSOL would provide more complete performance data but were not conducted. While these omissions do not undermine the core conclusions, that dual-stimulus control enables selective reconfiguration, they leave precise performance limits to be established in future studies.

Finally, all demonstrations employed open-loop manual control based on visual feedback. Practical medical applications would require closed-loop control integrating real-time position tracking and automated thermal activation to ensure safety and precision.

6 Conclusions and future work

This thesis presented a modular magnetic soft robotic system that integrates thermally reversible adhesion with magnetic actuation to enable selective locking, unlocking, and cooperative motion. The work establishes that dual-stimulus control (combining magnetic fields for locomotion and assembly with external RF heating for selective anchoring) provides a viable pathway toward reconfigurable multi-robot systems for minimally invasive medical applications.

The primary contributions of this work are threefold. First, the force hierarchy design principle was validated experimentally: cold-state EVA adhesion (5.40 N normal, 7.21 N shear) substantially exceeds robot–robot magnetic coupling (3.5 N), while hot-state adhesion drops to near zero, enabling reliable selective anchoring and release. This hierarchy ($F_{\text{adh,cold}} > F_{AB} > F_{\text{adh,hot}}$) proved robust across all demonstration experiments, with no unintended detachments or anchoring failures observed during two-robot, line, and ring assembly operations.

Second, the three-magnet asymmetric configuration successfully enabled multifunctional actuation from a single robot design. By arranging three N45SH magnets in a $(+, -, -)$ polarity sequence, individual robots achieved controlled rotation under uniform magnetic fields, while also enabling deformation through localised magnetic forces at compliant hinge points (53% height reduction demonstrated under gradient fields). Ring assemblies with one polarity-reversed robot generated net dipole moments sufficient for coherent collective rotation, demonstrating that geometric programming of magnetic interactions can coordinate multi-robot behaviour without requiring heterogeneous materials or robot-specific customisation.

Third, the thermal parameter screening identified a narrow but practical operating window for RF-activated EVA adhesion. The selected configuration (1.0 mm EVA, 48 µm aluminium foil, 1 cm coil distance) achieved controllable heating (40 s to 80°C) and cooling (80 s to 40°C) with adequate spatial selectivity (1 cm^2 heating spot) to target individual robots within assembled structures. The characterisation of failure modes (material overflow for thin EVA, robot sinking for thick EVA, and thermal overshoot for thick foil) established design principles that may inform future thermally activated interfaces: adhesive layer thickness should match the characteristic robot contact dimension to balance heating speed, geometric stability, and adhesive strength.

The demonstration experiments validated the system concept across progressively complex scenarios. Single-robot capabilities (rotation, translation, and deformation) were successfully demonstrated under both uniform and gradient magnetic fields. Multi-robot assemblies (lines of 6 robots, rings of 5–7 robots) formed through magnetic self-organisation without requiring precise positioning control. Selective thermal anchoring enabled sequential assembly construction: one robot could be fixed while others were magnetically manipulated, then specific robots could be selectively released or entire assemblies detached simultaneously. Collective rotation of asymmetric ring assemblies under uniform fields (10–30 mT, 0.05–0.2 Hz) demonstrated coherent multi-robot motion, though stability decreased for rings larger than 6–7 robots due to increased mass and gravitational loading on the compliant TPU structure.

The COMSOL simulations provided valuable design insight despite quantitative limitations. Simulations revealed that observable deformation requires field strengths exceeding 50 mT. This was confirmed experimentally: no visible deformation was observed when robots were subjected to the maximum uniform field (50 mT) in the Helmholtz coil, while the strong gradient field from the external cylindrical magnet achieved 53% height reduction. Robot–robot force predictions closely matched experimental measurements, validating the magnetic interaction model and providing confidence in the force hierarchy design. While the 2D plane-stress deformation model underestimated experimental height reduction (19% vs 53%), it successfully captured the qualitative physics (hinge bending, stress concentration at flexure points, and monotonic deformation with field strength) confirming the viability of the compliant hinge design concept.

Several promising directions emerge from this work. Most immediately, transitioning to biocompatible materials is essential for medical translation. Mucoadhesive coatings such as chitosan–glycerol blends represent a particularly promising avenue: these materials exhibit tunable adhesion to mucosal surfaces in the gastrointestinal and respiratory systems and could potentially be thermally activated using near-infrared (NIR) light or RF heating. Investigating the temperature-dependent adhesion strength, mechanical durability, and thermal reversibility of chitosan films on biological tissues would establish whether thermally switchable mucoadhesion can replicate the force hierarchy demonstrated here with EVA. Additionally, embedding thin aluminium or biocompatible conductive layers directly within polymer matrices could enable

RF heating without external metal components, though biocompatibility and long-term tissue response of embedded metals require thorough validation.

Beyond materials, integrating closed-loop control and medical imaging would enable autonomous operation. Real-time tracking of robot positions via ultrasound or magnetic resonance imaging could provide feedback for automated magnetic field planning and thermal activation scheduling. Machine vision or embedded force sensing could detect successful assembly formation and verify adhesion states, reducing reliance on operator judgment. Such integration would be essential for clinical deployment where precise, repeatable operation is critical for patient safety.

Exploring specific biomedical applications would provide concrete targets for system optimisation. Modular endoscopy where robots deploy sequentially through narrow working channels then assemble in situ could leverage the demonstrated selective anchoring for adaptive navigation and stable positioning during interventional procedures. Targeted drug delivery systems could exploit ring formation to encapsulate tissue targets, with thermal activation triggering both adhesion and drug release if thermally responsive carriers were integrated. Tissue grafting and temporary implant support represent another application domain: robots could position and mechanically support biological scaffolds during tissue integration, then be thermally disassembled and removed once healing is complete. Retrieval of foreign objects or tissue samples could utilize the deformation capability, with robots pinching to grasp irregular targets under gradient magnetic fields.

From a fundamental research perspective, several technical refinements would strengthen the platform. Three-dimensional COMSOL models with hyperelastic constitutive relations, contact mechanics, and realistic gradient field distributions would improve quantitative deformation predictions and enable design optimisation for specific gripping or navigation tasks. Material substitutions (softer elastomers (TPU Shore 65A or silicone), thinner wall sections, or optimised hinge geometries) could reduce the field strength threshold for pinching, potentially enabling deformation at the 10–50 mT levels compatible with clinical magnetic navigation systems. Investigating alternative magnetic configurations (e.g., magnetic polymer composites rather than discrete hard magnets) could reduce robot mass and improve biocompatibility while maintaining actuation performance. Scaling studies to determine maximum feasible assembly size and identify the dominant factors limiting stability (mass, compliance, surface friction, or magnetic coupling strength) would clarify design requirements for larger cooperative structures.

In conclusion, this thesis establishes the feasibility and fundamental operating principles of dual-stimulus control for reconfigurable magnetic soft robot assemblies. The force hierarchy design, thermal parameter optimisation, and assembly coordination strategies developed here provide a foundation for future research at the intersection of soft robotics, modular systems, and minimally invasive medical technology. While substantial development remains before clinical deployment, the successful integration of magnetic actuation with thermally reversible adhesion demonstrates a viable pathway toward selective, on-demand reconfiguration of cooperative robotic systems.

References

[1] Ziyu Ren and Metin Sitti. Design and build of small-scale magnetic soft-bodied robots with multimodal locomotion. *Nature protocols*, 19(2):441–486, 2024.

[2] Jiaqi Miao and Siqi Sun. Design, actuation, and functionalization of untethered soft magnetic robots with life-like motions: A review. *Journal of Magnetism and Magnetic Materials*, 586:171160, 2023.

[3] Adriana Vasi. Shape-morphing assembly and coordinated locomotion of magnetic soft robots for enhanced performance in navigating large cavities. Internship Report S5344883, University of Groningen, Surgical Robotics Laboratory, June 2023. Supervisor: prof. dr. S. Misra.

[4] Ren Hao Soon, Zhen Yin, Metin Alp Dogan, Nihal Olcay Dogan, Mehmet Efe Tiryaki, Alp Can Karacakol, Asli Aydin, Pouria Esmaeili-Dokht, and Metin Sitti. Pangolin-inspired untethered magnetic robot for on-demand biomedical heating applications. *Nature Communications*, 14(1):3320, 2023.

[5] Xili Lu, Hu Zhang, Guoxia Fei, Bing Yu, Xia Tong, Hesheng Xia, and Yue Zhao. Liquid-crystalline dynamic networks doped with gold nanorods showing enhanced photocontrol of actuation. *Advanced Materials*, 30(14):1706597, 2018.

[6] Shuang Wu, Gregory Langston Baker, Jie Yin, and Yong Zhu. Fast thermal actuators for soft robotics. *Soft Robotics*, 9(6):1031–1039, 2022.

[7] Xiaofan Luo, Kathryn E Lauber, and Patrick T Mather. A thermally responsive, rigid, and reversible adhesive. *Polymer*, 51(5):1169–1175, 2010.

[8] Ziheng Chen, Yibin Wang, Hui Chen, Junhui Law, Huayan Pu, Shaorong Xie, Feng Duan, Yu Sun, Na Liu, and Jiangfan Yu. A magnetic multi-layer soft robot for on-demand targeted adhesion. *Nature Communications*, 15(1):644, 2024.

[9] Zhengxin Yang and Li Zhang. Magnetic actuation systems for miniature robots: A review. *Advanced Intelligent Systems*, 2(9):2000082, 2020.

[10] Nafiseh Ebrahimi, Chenghao Bi, David J Cappelleri, Gastone Ciuti, Andrew T Conn, Damien Faivre, Neda Habibi, Alexander Hošovskỳ, Veronica Iacovacci, Islam SM Khalil, et al. Magnetic actuation methods in bio/soft robotics. *Advanced Functional Materials*, 31(11):2005137, 2021.

[11] Chen Wang, Aldona Mzyk, Romana Schirhagl, Sarthak Misra, and Venkatsubramanian Kalpathy Venkiteswaran. Biocompatible film-coating of magnetic soft robots for mucoadhesive locomotion. *Advanced Materials Technologies*, 8(12):2201813, 2023.

[12] Clio Siebenmorgen, Chen Wang, Laurens Bosscher Navarro, Daniele Parisi, Sarthak Misra, Venkatasubramanian Kalpathy Venkiteswaran, and Patrick van Rijn. Minimally designed thermo-magnetic dual responsive soft robots for complex applications. *Journal of Materials Chemistry B*, 12(22):5339–5349, 2024.

[13] Steven Floyd, Eric Diller, Chytra Pawashe, and Metin Sitti. Control methodologies for a heterogeneous group of untethered magnetic micro-robots. *The International Journal of Robotics Research*, 30(13):1553–1565, 2011.

[14] Min Wang, Tianyi Wu, Rui Liu, Zhuoran Zhang, and Jun Liu. Selective and independent control of microrobots in a magnetic field: a review. *Engineering*, 24:21–38, 2023.

[15] Soichiro Tottori, Naohiko Sugita, Reo Kometani, Sunao Ishihara, and Mamoru Mitsuishi. Selective control method for multiple magnetic helical microrobots. *Journal of Micro-Nano Mechatronics*, 6(3):89–95, 2011.

[16] Pranay Mandal, Vaishali Chopra, and Ambarish Ghosh. Independent positioning of magnetic nanomotors. *ACS nano*, 9(5):4717–4725, 2015.

[17] Jessica A-C Liu, Jonathan H Gillen, Sumeet R Mishra, Emily E Evans, and Joseph B Tracy. Photothermally and magnetically controlled reconfiguration of polymer composites for soft robotics. *Science advances*, 5(8):eaaw2897, 2019.

[18] Fu Zhao, Weibin Rong, Lefeng Wang, and Lining Sun. Photothermal-responsive shape-memory magnetic helical microrobots with programmable addressable shape changes. *ACS Applied Materials & Interfaces*, 15(21):25942–25951, 2023.

[19] Anil K Bastola and Mokarram Hossain. A review on magneto-mechanical characterizations of magnetorheological elastomers. *Composites Part B: Engineering*, 200:108348, 2020.

[20] Venkatasubramanian Kalpathy Venkiteswaran and Sarthak Misra. Towards gradient-based actuation of magnetic soft robots using a six-coil electromagnetic system. In *2020 IEEE/RSJ International Conference on Intelligent Robots and Systems (IROS)*, pages 8633–8639. IEEE, 2020.

[21] Jinsong Leng, Xin Lan, Yanju Liu, and Shanyi Du. Shape-memory polymers and their composites: stimulus methods and applications. *Progress in Materials Science*, 56(7):1077–1135, 2011.

A Geometry comparison and design trade-offs

Four candidate robot geometries were considered during conceptual design: circular, triangular, square, and hexagonal. Each shape was evaluated against four criteria: rotational symmetry (for steering), tessellation (for assembly), magnet accommodation, and stress distribution.

Table 5: Comparison of candidate robot geometries. ✓ = favourable; × = limitation.

Criterion	**Circular**	**Square**	**Triangular**	**Hexagonal**
Rotational symmetry	✓	×	×	✓
Magnet embedding surface	×	✓	✓	✓
Tessellation ability	×	✓	✓	✓
Stress distribution	✓	×	×	✓
Assembly flexibility	×	✓	×	✓
Fabrication simplicity (3D printing)	✓	✓	✓	✓
Overall suitability	Moderate	Moderate	Limited	**High**

Discussion The hexagonal robot achieved the best balance across all criteria. It combines nearly isotropic rotation with perfect tessellation, offers flat embedding surfaces for magnet alignment, and demonstrates improved stress distribution during cyclic deformation. Circular geometries provided smooth rotation but poor assembly control, while triangular and square designs limited interconnection modes or produced excessive stress concentrations at corners. For these reasons, the hexagon was selected as the final geometry for all subsequent fabrication and testing.

B Analytical derivation of the net dipole moment

The robot contains three magnets embedded in faces 0, 2, and 4 of a regular hexagon, at angles

$$\theta_0 = 0^\circ, \qquad \theta_2 = 120^\circ, \qquad \theta_4 = 240^\circ.$$

The polarity assignment is $s_0 = +1$ (north pole outward) and $s_2 = s_4 = -1$ (north poles inward). The net dipole moment $\mathbf{m}_{\text{net}}$ is the vector sum of the individual contributions.

Using unit normal vectors

$$\mathbf{n}(\theta) = \begin{bmatrix} \cos\theta \\ \sin\theta \end{bmatrix},$$

the normal directions of the three magnet-bearing faces are

$$\mathbf{n}(\theta_0) = \mathbf{n}(0^\circ) = \begin{bmatrix} 1 \\ 0 \end{bmatrix},$$

$$\mathbf{n}(\theta_2) = \mathbf{n}(120^\circ) = \begin{bmatrix} -\frac{1}{2} \\ \frac{\sqrt{3}}{2} \end{bmatrix} \approx \begin{bmatrix} -0.5 \\ 0.87 \end{bmatrix},$$

$$\mathbf{n}(\theta_4) = \mathbf{n}(240^\circ) = \begin{bmatrix} -\frac{1}{2} \\ -\frac{\sqrt{3}}{2} \end{bmatrix} \approx \begin{bmatrix} -0.5 \\ -0.87 \end{bmatrix}.$$

Each magnet contributes a dipole $s_i m_0 \mathbf{n}(\theta_i)$, so

$$\begin{aligned}\frac{\mathbf{m}_{\text{net}}}{m_0} &= s_0\mathbf{n}(\theta_0) + s_2\mathbf{n}(\theta_2) + s_4\mathbf{n}(\theta_4) \\ &= (+1)\begin{bmatrix}1\\0\end{bmatrix} + (-1)\begin{bmatrix}-\frac{1}{2}\\ \frac{\sqrt{3}}{2}\end{bmatrix} + (-1)\begin{bmatrix}-\frac{1}{2}\\ -\frac{\sqrt{3}}{2}\end{bmatrix} \\ &= \begin{bmatrix}1\\0\end{bmatrix} + \begin{bmatrix}0.5\\ -\frac{\sqrt{3}}{2}\end{bmatrix} + \begin{bmatrix}0.5\\ \frac{\sqrt{3}}{2}\end{bmatrix} \\ &= \begin{bmatrix}2\\0\end{bmatrix}.\end{aligned}$$

Thus, the resultant dipole is

$$\mathbf{m}_{\text{net}} = 2m_0\hat{\mathbf{x}},$$

directed along the axis of Face 0. In the figure, this corresponds to

$$\mathbf{m}_0 = m_0[1,\, 0], \quad \mathbf{m}_2 = m_0[0.5,\, -0.87], \quad \mathbf{m}_4 = m_0[0.5,\, 0.87],$$

whose vector addition yields $\mathbf{m}_{\text{net}} = 2m_0\hat{\mathbf{x}}$.

C Material specifications

This appendix summarises the relevant mechanical and magnetic properties of the materials used for the robot body and for the permanent magnets embedded in the robots or used for external actuation. All values are taken from manufacturer datasheets.

Thermoplastic Polyurethane (TPU-85A)

Table 6: Material properties of TPU-85A (robot body).

Property	**Value**
Shore hardness	85A
Density	1.21 g/cm^3
Tensile modulus	10–12 MPa
Elongation at break	$> 400\%$
Glass transition temperature T_g	-30°C
Melting range	180–200°C
Maximum recommended service temperature	> 100°C
Thermal conductivity	0.20 W/mK
Notes	Flexible, resilient.

N45SH block magnet (embedded robot magnets)

Table 7: Material properties of the N45SH block magnets (5 mm × 4 mm × 1 mm) embedded in the robots.

Property	**Value**
Material	NdFeB (Grade N45SH)
Dimensions	5 mm × 4 mm × 1 mm
Coating	Zinc plated (Zn)
Remanent flux density B_r	1.35 T
Coercivity H_c	955 kA/m
Maximum operating temperature	150°C
Magnetisation direction	Through thickness (1 mm)
Volume	2.0×10^{-8} m^3
Dipole moment (per magnet)	2.15×10^{-2} A · m^2
Holding force (manufacturer)	$\sim$ 0.34 kg ($\sim$ 3.3 N)
Notes	High coercivity; stable during thermal cycles used in this work.

N45 Cylindrical actuation magnet (external handheld magnet)

Table 8: Material properties of the external cylindrical N45 magnet (35 mm diameter, 20 mm height).

Property	**Value**
Material	NdFeB (Grade N45)
Shape	Cylinder
Dimensions	Diameter 35 mm, Height 20 mm
Coating	Ni–Cu–Ni (triple layer nickel)
Magnetisation direction	Axial (parallel to height)
Remanent flux density B_r	$\sim$ 1.32–1.35 T
Maximum operating temperature	80°C
Weight	150 g
Holding force (manufacturer)	$\sim$ 38 kg ($\sim$ 373 N)
Shear force	$\sim$ 7.7 kg ($\sim$ 75.4 N)
Notes	Used as the handheld actuation magnet to generate translation and peeling forces.

D Force sensor and calibration details

Magnetic force measurements described in Section 3.6.2 were performed using a K3D40 three-axis force sensor. The 10 N per-axis range and low crosstalk of the sensor make it suitable for resolving both the relatively small robot–robot interaction forces and the larger forces generated by the handheld cylindrical magnet during robot–magnet tests.

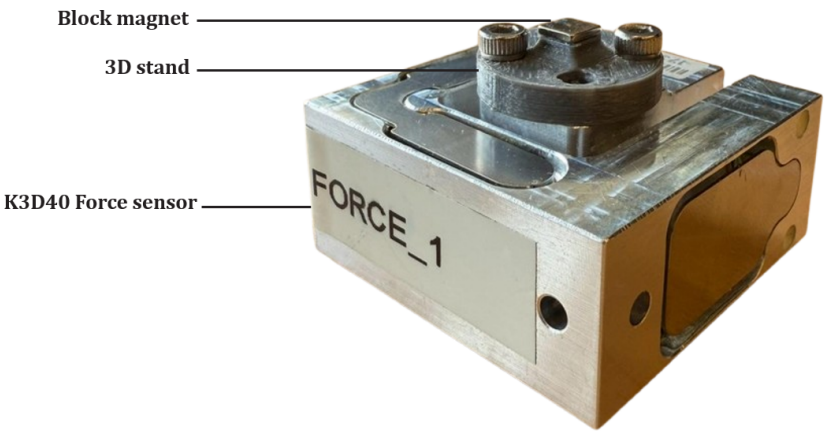

Figure 36: Force measurement setup. A single N45SH block magnet is mounted on a PLA fixture and fixed to the K3D40 three-axis force sensor. The Z-stage controls the separation distance during robot–robot and robot–magnet force measurements.

Sensor specifications

The sensor housing measures $40 \times 40 \times 20$ mm and incorporates three orthogonally arranged double cantilever beams with full-bridge strain gauges. Vector decomposition is therefore performed mechanically, with remaining transverse loads compensated electrically through the Wheatstone bridges.

Table 9: Technical specifications of the K3D40 10N force sensor (manufacturer datasheet).

Property	**Value**	**Unit**
Rated force (Fx, Fy, Fz)	10	N
Accuracy class	0.5	—
Relative linearity error	0.2	%FS
Crosstalk (Fx→Fy, Fy→Fx)	0.5	%FS
Crosstalk (Fz→Fx/Fy)	0.5	%FS
Crosstalk (Fx/Fy→Fz)	2.5	%FS
Rated output	0.5	mV/V
Input/Output resistance	350	Ω
Operating temperature range	–20 to 70	°C
Natural frequency	~ 1	kHz
Material	Aluminium alloy	—

Mounting and fixtures

A custom 3D-printed PLA stand was used to secure the robot (or single block magnet) to the sensor surface while preventing unwanted tilting moments. The stand was attached using two M3 screws through the threaded mounting holes of the sensor.

Amplifier and data acquisition

Signals were read using a GSV-4USB measurement amplifier at 10 Hz. Before each run, the system was zeroed for 5 s to eliminate thermal drift. Force values were exported as CSV files and processed in Python for averaging and smoothing.

Environmental conditions

All measurements were performed under standard laboratory conditions (22–25°C, ambient humidity), with no additional magnetic shielding. The acrylic base used in the setup ensured that no magnetic interference or structural deformation occurred during loading.

E Thermal screening dataset

This appendix contains the full dataset from the thermal parameter study described in Section 3.6.3. A total of 36 combinations of EVA thickness, aluminium foil thickness, and coil–substrate distance were tested to evaluate heating performance under RF excitation. For each configuration, the following quantities were recorded where applicable:

- t_{80}: time to reach 80°C,
- t_{100}: time to reach 100°C (only when reached),
- $T_{\max}$: maximum temperature observed,
- t_{cool}: cooling time from $T_{\max}$ to 40°C.

Entries marked "—" indicate conditions where the target temperature was not reached or no value was recorded. Table 10 summarises all 36 measurements. The structure follows the testing order, and the Notes column provides a concise qualitative description of the heating behaviour for each configuration.

Table 10: Thermal screening dataset for all parameter combinations. A total of 36 configurations were tested by varying EVA thickness, aluminium foil thickness, and coil–substrate distance.

Run ID	**EVA** (mm)	**Foil** (μm)	**Coil** (cm)	t_{80} (s)	t_{100} (s)	$T_{\max}$ (°C)	t_{cool} (s)	**Notes**
1	0.5	16	1	—	—	—	—	Insufficient heating; did not reach 80°C
2	0.5	16	2	>120	>120	—	120	Reached ∼70°C only within 120 s
3	0.5	16	3	>120	>120	—	—	Very weak coupling; minimal temperature rise
4	0.5	16	5	>120	>120	—	—	No meaningful heating observed
5	0.5	48	1	12	20	—	—	Fast heating; reached 80°C and 100°C quickly
6	0.5	48	2	>120	>120	70	120	Reached ∼70°C after 3 min; below target
7	0.5	48	3	>120	>120	—	—	Insufficient heating at this distance
8	0.5	48	5	>120	>120	—	—	Very weak response; did not reach 80°C
9	0.5	100	1	8	16	—	72	Very fast heating; strong coupling, risk of overshoot
10	0.5	100	2	>120	>120	—	—	Heating insufficient at larger distance
11	0.5	100	3	>120	>120	—	—	Minimal effect within measurement window
12	0.5	100	5	>120	>120	—	—	No effective heating observed
13	1.0	16	1	64	80	—	72	Slow but usable heating at short distance
14	1.0	16	2	>120	>120	—	72	Did not reach 80°C; marginal coupling
15	1.0	16	3	>120	>120	—	72	Very slow response; below useful heating range
16	1.0	16	5	>120	>120	—	72	No practical heating at this distance
17	1.0	48	1	40	55	115	80	**Selected configuration: fast, repeatable response**
18	1.0	48	2	78	252	95	—	Slow but reaches target; noticeable overshoot
19	1.0	48	3	>120	>120	—	—	Too slow; did not reach 80°C reliably
20	1.0	48	5	>120	>120	26	—	Barely exceeds ambient temperature
21	1.0	100	1	13	19	110	—	Very fast heating; significant overshoot risk
22	1.0	100	2	>240	>240	—	—	Unstable behaviour; stopped before reaching 80°C
23	1.0	100	3	>120	>120	—	—	Inefficient heating at this spacing
24	1.0	100	5	>120	>120	29	—	Only small temperature increase after 2 min
25	2.0	16	1	178	310	—	—	Very slow heating through thick EVA layer
26	2.0	16	2	>120	>120	—	—	Did not reach 80°C; poor coupling
27	2.0	16	3	>120	>120	—	—	Insufficient heating for thick EVA at this distance
28	2.0	16	5	>120	>120	—	—	No meaningful heating observed
29	2.0	48	1	52	90	—	—	Acceptable heating; slower due to thick EVA
30	2.0	48	2	112	220	—	—	Slow heating; upper limit of practical times
31	2.0	48	3	>120	>120	—	—	Did not reach 80°C in measurement window
32	2.0	48	5	>120	>120	—	—	Very slow; unsuitable for operation
33	2.0	100	1	34	49	—	—	Fast heating but overshoot risk with thick EVA
34	2.0	100	2	130	270	—	—	Long heating times; not practical
35	2.0	100	3	>120	>120	—	—	Target temperature not reached
36	2.0	100	5	>120	>120	—	—	Very poor heating performance

F Single-magnet deformation analysis

To understand the individual contribution of each bottom magnet to robot deformation, simulations were performed with only one bottom magnet activated at a time: (i) left bottom magnet only (face 2, north pole inward), and (ii) right bottom magnet only (face 4, north pole inward).

Figure 37 shows representative deformation fields for the right-magnet case across field strengths from 10 to 200 mT. No visible deformation was observed below 50 mT in either simulation case.

The vertical displacement quantification reveals that below 100 mT, the left and right cases exhibit similar deformation. Beyond 100 mT, the curves diverge: the right-magnet case reaches 2.74 mm at 200 mT (13.8% height reduction), while the left-magnet case reaches 1.55 mm at 200 mT (7.8% height reduction). This asymmetry arises from the geometric positioning of the magnets and the constraint conditions, but since the robot always operates with all three magnets active in practice, the net-dipole loading case (Section 4.4.1) is most relevant to system performance.

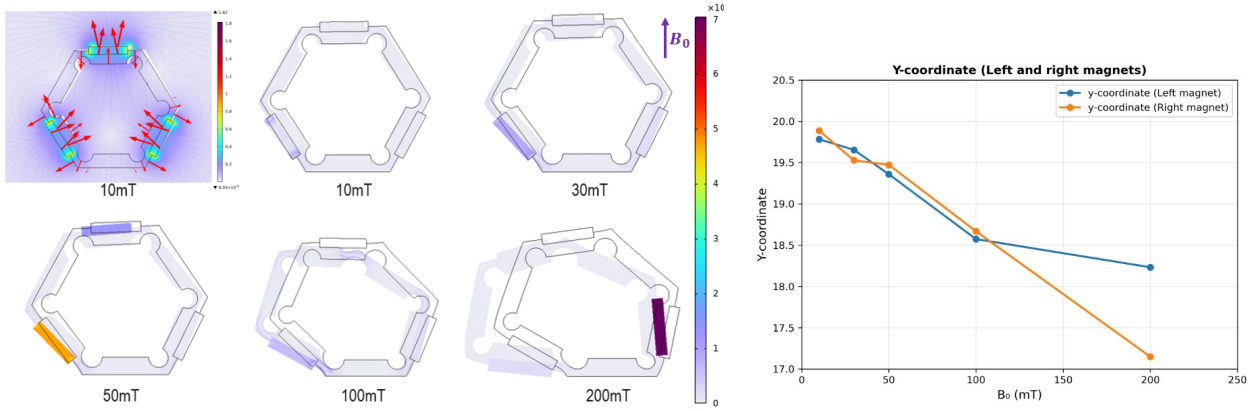

(a) Deformation progression

(b) Vertical displacement vs. B_0

Figure 37: Single-magnet loading analysis with only the right bottom magnet active (face 4). (a) COMSOL deformation showing von Mises stress distribution for $B_0 = 10, 30, 50, 100, 200$ mT. (b) Vertical displacement comparing left (blue) vs. right (orange) magnet activation.